MAGMATIC UNDER-PLATING BENEATH THE LUANGWA RIFT VALLEY, ZAMBIA?

By

KITSO NKOOKO MATENDE

Bachelor of Science in Applied Geophysics

University of Botswana

Gaborone, Botswana

2013

Submitted to the Faculty of the
Graduate College of the
Oklahoma State University
in partial fulfillment of
the requirements for
the Degree of
MASTER OF SCIENCE
May, 2015

MAGMATIC UNDER-PLATING BENEATH THE LUANGWA RIFT VALLEY, ZAMBIA?

Thesis Approved:

Dr. Estella A. Atekwana

Thesis Adviser

Dr. Mohamed G. Abdelsalam

Dr. Daniel A. Laó-Dávila

ACKNOWLEDGEMENTS

I would like to express my sincere gratitude to my advisor Dr. Estella Atekwana for her supervision, encouragement and coaching. Without her help, this work would not have been possible. Many thanks are due to my committee members, Dr. Mohamed Abdelsalam and Dr. Daniel A. Laó-Dávila for their recommendations in improving my thesis. In addition, to Dr. Abdelsalam, thank you very much for your open-door policy, and the tremendous amount of time you dedicate to students. Special thanks go to Dr. Kevin Mickus of Missouri State University for his major inputs and contributions to my project.

This project is funded by the National Science Foundation – Continental Dynamics grant # EAR 1255233 “Integrated Studies of Continental Rifting: From Nascent Extension (Okavango Rift Zone) to Continental Breakup (Afar Depression)”. Student financial support is provided by the Geological Society of America (GSA). I would like to thank Oklahoma State University and the Boone Pickens School of Geology for the excellent quality of education they offered me. I am also grateful for the scholarships awarded to me. These include the RE and KR McPhail Geology Scholarship.

Khumo Leseane, Kathleen Robertson and Landon Lockhart helped with field work and the University of Zambia provided logistical support. Dr. O. Sikazwe and Dr. I. Nyambe were instrumental in obtaining permits for work within National Parks. Thanks also go to Mr Willie Nundwe and Philip Sikazwe for their help in the field.

I would like to forward my special thanks to my family, especially my mother (Eva S. Matende), sisters (Lorato Gabaleswe, Dina Mabechu, and Mmabatho Matende) and brother (Mogomotsi Tladi), for their endless supply of encouragement and support throughout this project. Special thanks also go to my friends who have been a constant source of encouragement, among them, Khumo Leseane, Otlaadisa Tafila, Andrew Katumwehe.

Name: KITSO NKOOKO MATENDE

Date of Degree: MAY, 2015

Title of Study: MAGMATIC UNDER-PLATING BENEATH THE LUANGWA RIFT VALLEY, ZAMBIA?

Major Field: GEOLOGY

Abstract:

We used aeromagnetic data, and satellite and terrestrial gravity data to examine the thermal and crustal structure beneath the Karoo-aged Luangwa Rift Valley (LRV) in Zambia in order to determine the geodynamic controls of its formation. We computed Curie Point Depth (CPD) values using two-dimensional (2D) power spectrum analysis of the aeromagnetic data, and these results were used to calculate heat flow under the LRV. We also inverted the aeromagnetic data for three-dimensional (3D) magnetic susceptibility distribution. We further determined the crustal thickness beneath the LRV by calculating depths to the Moho using 2D power spectrum analysis of the satellite gravity data. We found that: (1) there is no elevated CPD beneath the LRV, and as such no elevated heat flow anomaly. (2) there are numerous 5-15 km wide magnetic bodies at shallow depth (5-20 km) under the LRV. (3) the Moho beneath the LRV is 50 km deep, compared to 35-45 km depths outside the rift. The gravity-derived Moho depths beneath the LRV differ from Moho depths determined from preliminary results of passive seismic studies but are comparable with those outside the rift. (4) there is a broad long-wavelength positive anomaly in the terrestrial gravity data, possibly related to the presence of dense material at the Moho level. This anomaly is modified by shorter-wavelength positive anomalies at the rift shoulders and floor that might be related to shallow depth magnetic bodies. Also, there are negative short-wavelength anomalies that correlate with rift sediment infill. We subsequently used the ground gravity data to develop 2D forward models to reconcile the observed thermal and crustal characteristics of the LRV. Our models suggest that the deeper Moho beneath the rift is due to the presence of a magmatic under-plated mafic body. The difference between the gravity and passive seismic Moho depths estimates may be because the passive seismic data imaged the top of the under-plated mafic body whereas the gravity data imaged the base. Magmatic under-plating may have introduced a rheological weakness that facilitated strain localization during rift initiation.

TABLE OF CONTENTS

Chapter Page

LIST OF TABLES

Table Page

LIST OF FIGURES

CHAPTER I

INTRODUCTION

Continental rifts form elongated depressions on the Earth's surface that result from extension of the Earth's lithosphere (e.g., Tommasi and Vauchez, 2001; Thybo and Nielsen, 2009). Some areas within continents appear to be more vulnerable to rifting than others (Lynch and Morgan, 1987). Hence, understanding rift initiation requires a clear comprehension of the processes that control the localization of extension. Knowledge of such processes is limited and especially in magma poor rifts remains a matter of much debate and uncertainty (e.g., Keranen et al., 2004; Keir et al., 2006, and references therein; Koptev et al., 2015).

Analogue and numerical modeling by Corti et al. (2002) and Buck (2006) suggest that magma thermally weakens the continental lithosphere, making it easier to rift. These magma-assisted rifting models are supported by the observed occurrence of magmatism throughout the Eastern Branch of the East African Rift System (EARS) and the Main Ethiopian Rift (MER). In these models, strain is localized by magmatic intrusions and faulting (Ebinger and Casey, 2001; Keranen et al., 2004; Casey et al., 2006; Ebinger et al., 2008; Ebinger et al., 2010). Callot et al. (2001) demonstrated by analogue modeling that strain localization can also be controlled by low viscosity bodies interpreted as partially melted regions located in the lower crust and upper mantle. In some portions of the largely amagmatic Western Branch of the EARS, strain localization may be achieved through plume-related melts imaged as zones of low seismic velocities in the upper mantle and lower crust (Wolbern et al., 2010; Jakovlev et al., 2011). In the Okavango Rift Zone, the youngest segment of the EARS, Leseane et al. (2015) suggested that the strain is localized through ascending mantle fluids facilitated by the presence of lithospheric-scale Precambrian structures that served as a conduit to the rising mantle fluids.

Rift propagation tends to follow the general trend of the pre-existing fabric, or zones of weaknesses, at various scales (e.g., Daly et al., 1989; Birt et al., 1997; Tommasi and Vauchez, 2001; Acocella et al., 2004; Morley et al., 2004). At regional scales, the occurrence of rifting within orogenic belts as opposed to the adjacent cratons is due to differences in lithospheric thicknesses and fault densities in orogenic belts (e.g., McConnell, 1972; Ritsema et al., 1998). For example, the EARS (Fig. 1) bifurcates into two branches around the thick Tanzania Craton, with the Eastern and Western Branches largely occurring within the thinner and much weaker lithospheres of the Mozambique and Ubendien orogenic belts, respectively. The differences in the lithospheric thickness have also been attributed to the observed variation in heat flow distribution, with the thick cratons generally being colder than the thinner orogenic belts (Ballard and Pollack, 1987). Ballard and Pollack (1987) suggest that this difference is due to the diversion of heat away from the cratons into the surrounding thinner orogenic belts by lithosphere roots, and edge-driven convection cells beneath the orogenic belts. van Wijk et al. (2010) have suggested the differences in lithospheric thicknesses between the thick Colorado Plateau (~120-140 km) and the thinner surrounding Rio Grande rift and Basin and Range province to have set up edge-driven convection cells, and thus localizing strain within the two extensional structures.

At local scales, faults and shear zones play an important role in strain localization during rifting (e.g., Daly et al., 1989; Korme et al., 2004). In the Western Branch of the EARS, strain localization in the Albertine Graben is facilitated by NE-trending Precambrian structures, while propagation of the Rhino Graben is terminated against the Precambrian structures associated with the NW-trending Aswa Shear Zone (Katumwehe et al., 2015). In addition, within the ORZ strain localization may have been facilitated at the suture between the Damara and Ghanzi-Chobe belts (Leseane et al., 2015). The development and evolution of the Rhine Graben (central Europe) were controlled, in part, by pre-existing crustal zones of weakness that were reactivated by the collision of the Eurasia and African plates during the Alpine orogeny (Illies, 1972; Fairhead and Stuart, 1982; Rousset et al., 1993; Schumacher, 2002; Dezes et al., 2004; Rotstein et al., 2006)

In addition to the above discussed modes of localization of extension, analogue modeling by Yamasaki and Gernigon (2009) has suggested under-plated mafic bodies (UPMBs) to play a crucial role in strain localization during rifting. The UPMBs, which may be emplaced before or during extension of the lithosphere, may introduce a rheological heterogeneity that localizes strain leading to rift development by either having an anomalously high temperature or having a mafic crustal composition that is significantly weaker than the mantle (Yamasaki and Gernigon, 2009). Depending on the size of the UPMBs, the temperature anomaly disappears within a few million years of emplacement but the rheological heterogeneity due to differences in composition between the UPMBs and the mantle can have an effect in localizing strain at any stage of extension (Yamasaki and Gernigon, 2009).

The Luangwa Rift Valley (LRV) is a Karoo-aged (Permian-Jurassic) rift occurring within the Irumide belt, a Mesoproterozoic-Neoproterozoic orogenic belt in eastern Zambia. The LRV follows the general NE-trending Precambrian structures [Fig. 3B]. The Precambrian Mwembeshi Shear Zone (Mw.S) occurs obliquely to the LRV, and has been suggested to have played an important role in localizing strain during rift initiation (Daly et al., 1989; Orpen et al., 1989; Banks et al., 1995). Observed in the LRV is the absence of any surficial magmatism. The origin of thermal springs that occur within and outside the rift has been attributed, through geochemical studies, to groundwater percolating through deep faults and heated by the normal geothermal gradient (Legg, 1974; Sakungo, 1985). These observations make the LRV an ideal place to examine different mechanisms of strain localization during the initiation of largely amagmatic rifts. Also, studies in the LRV are limited and there is no studies to date that examine the crustal structure of the LRV. Here, we use aeromagnetic, satellite and ground gravity data to investigate the crustal and thermal structure beneath the LRV in order to determine the geodynamic controls of the formation of the rift.

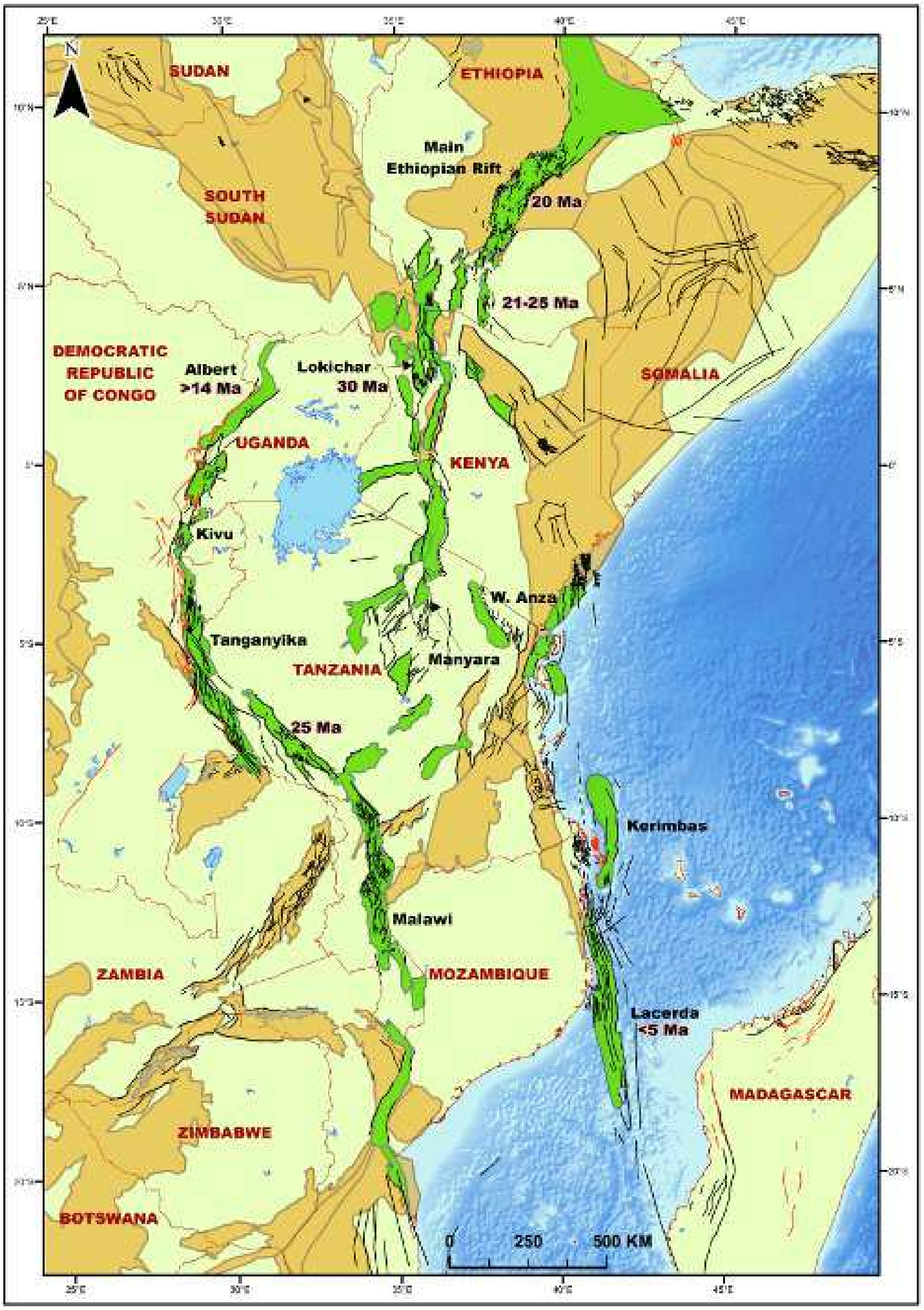

Figure 1: Map of the East African Rift System (EARS) in green, showing the main fault patterns and ages of rift initiation. Older Karoo basins are shown in orange (Source: GEO International).

CHAPTER II

TECTONIC SETTING

Two episodes of rifting have occurred in Eastern Africa. The first episode occurred during the Permian-Jurassic periods during the breakup of Gondwana, and resulted in the development of Karoo basins (Delvaux, 1989; Bumby and Guiroud, 2005; Catuneanu et al., 2005), which are largely confined to present-day south-central Africa and India (Rogers et al., 1995). The second rifting event began in the Cenozoic and resulted in the formation of the EARS (e.g., Mulibo and Nyblade, 2013). Fig. 1 shows the distribution of the EARS and the older Karoo rifts.

The early Permian rifting is associated with compressional/collision tectonics in southern Gondwana that reactivated the pre-existing Mwembeshi shear zone (Mw.S) with sinistrial movement (Daly et al., 1989; Orpen et al., 1989; Banks et al., 1995). The Ruhuhu (Tanzania), Luano and Lukusashi (Zambia), Aranos (Namibia) and Passarge (Botswana) basins were formed at the same time. The 3,500 km long steeply dipping Precambrian Mw.S forms a continental scale structure extending from the Damaran belt of Namibia in the SW, to Malawi in the NE (Daly et al., 1989; Rogers et al. (1995) and references therein). Its extension to the east is largely obscured by Karoo sediments

(Rogers et al., 1995). Mw.S forms the boundary between the Irumide and Southern Irumide belts.

In the Late Permian, dextral movements on the Mw.S caused inversion in most of the Karoo basins (Banks et al., 1995). Banks et al. (1995) postulated that during the breakup of Gondwana in the early Jurassic, changes in stress in the African continent, associated with the rearrangement of seafloor spreading patterns in the Indian and Atlantic oceans, were accommodated along different major zones of weakness such as the Mw.S. These changes in stress renewed left-lateral movement along Mw.S, which led to further extension of the LRV. The breakup of Gondwana was accompanied by volcanism that formed the Karoo Igneous Province, which is among the largest continental flood basalt provinces (Erlank, 1984; Cox, 1988; Duncan et al., 1997; Pálfy and Smith, 2000; Riley et al., 2005). The localization of the central and southern African Karoo basins along the Mw.S suggests that the shear zone played an important role in their development. Previous studies (e.g., Rosendahl, 1987; Delvaux et al., 1992; Ring, 1994; Mulibo and Nyblade, 2013) have suggested the Karoo rifts to have structurally influenced the Cenozoic rifting events. The newer rifts, however, do not always follow the Karoo rifts. The Bangweulu Block, an Archean craton (Drysdall et al., 1972; Andersen and Unrug, 1984; Daly et al., 1989; De Waele et al., 2006; O’Donnell et al., 2013) with a lithospheric thickness of ~150-200 km (O’Donnell et al., 2013) occurs to the north of the Irumide belt. To the northeast, the Irumide belt is truncated by faults and shear zones within the reactivated Palaeoproterozoic Ubendian belt (De Waele et al., 2009).

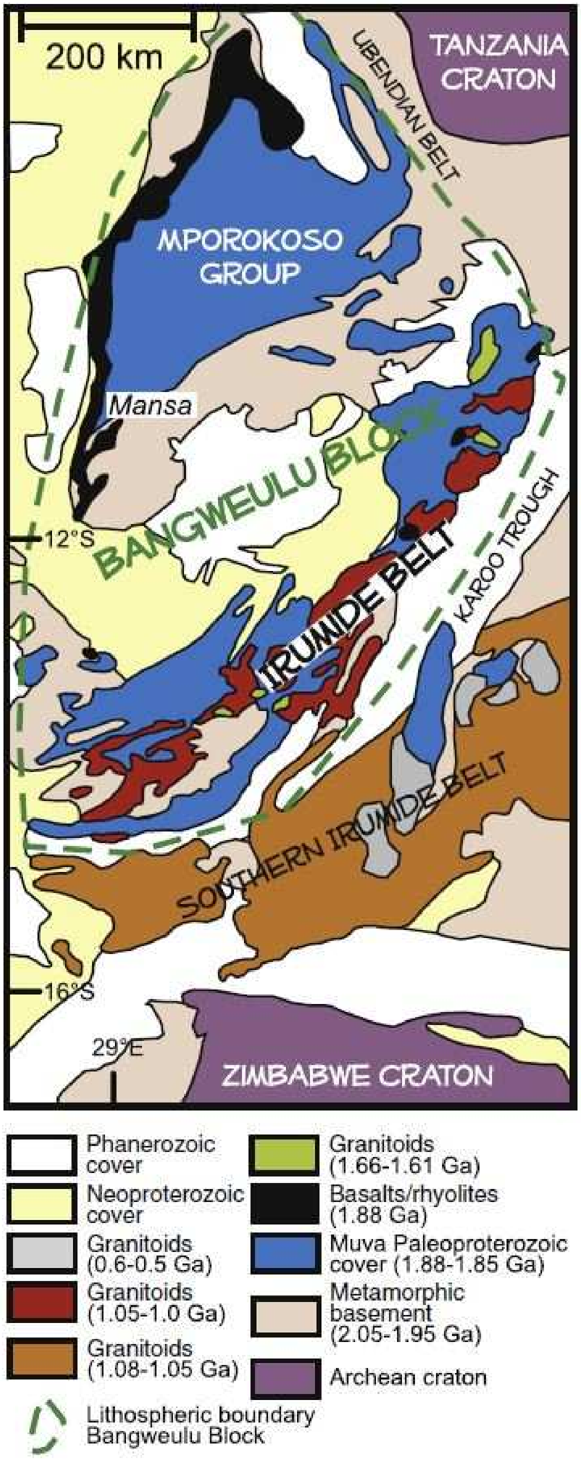

Figure 2: Geologic map of eastern Zambia (adopted from Liégeois et al., 2013).

The Mesoproterozoic Mporokoso basin occurs over the Bangweulu Block and contains up to 5 km of shallow marine and fluvial sediments (Andews-Speed, 1986). Geologically, the Irumide belt consists of unmetamorphosed clastic sedimentary rocks, high grade metamorphic amphibolite, highly deformed gneisses and metasedimentary rocks (e.g., De Waele and Mapani, 2002). The Southern Irumide belt occurs to the southeast of the Irumide belt (Daly et al., 1989; Orpen et al., 1989). In addition to Archean remnants, the Irumide belt is intruded by amphibolite-facies granitoids of various ages [Fig. 2] (Liégeois et al., 2013). Liégeois et al. (2013) suggest the Irumide belt to represent the southern metacratonic margin of the Bangweulu Block. The southern Irumide belt is on the other hand consists of granitoids without any occurrence of Archean remnants.

2.1 The Luangwa Rift Valley (LRV)

The ~600 km long and ~80 km wide Karoo-aged LRV occurs at the boundary between the NE-trending Mesoproterozoic-Neoproterozoic Irumide and Southern Irumide orogenic belts [Fig. 2]. The Lukusashi and Luano rift basins, also of Karoo-age, occur SW of LRV (Fig. 3). The LRV and Luano basins consist of up to 8 km and 2 km of Permo-Triassic clastic sediments of the Karoo Supergroup, respectively (Daly et al., 1989; Banks et al., 1995). Active rifting in the LRV began in the Early Permian and continued into the Triassic (Banks et al., 1995). The LRV comprises of two non-overlapping opposing half grabens separated by a structural high suggested to be a major splay of the Mw.S [Fig. 3B] (Daly et al., 1989; Banks et al., 1995). The northern sub-basin has its major bounding fault towards the east, while in the southern sub-basin the bounding fault occurs to the west [Fig. 3 and 4].

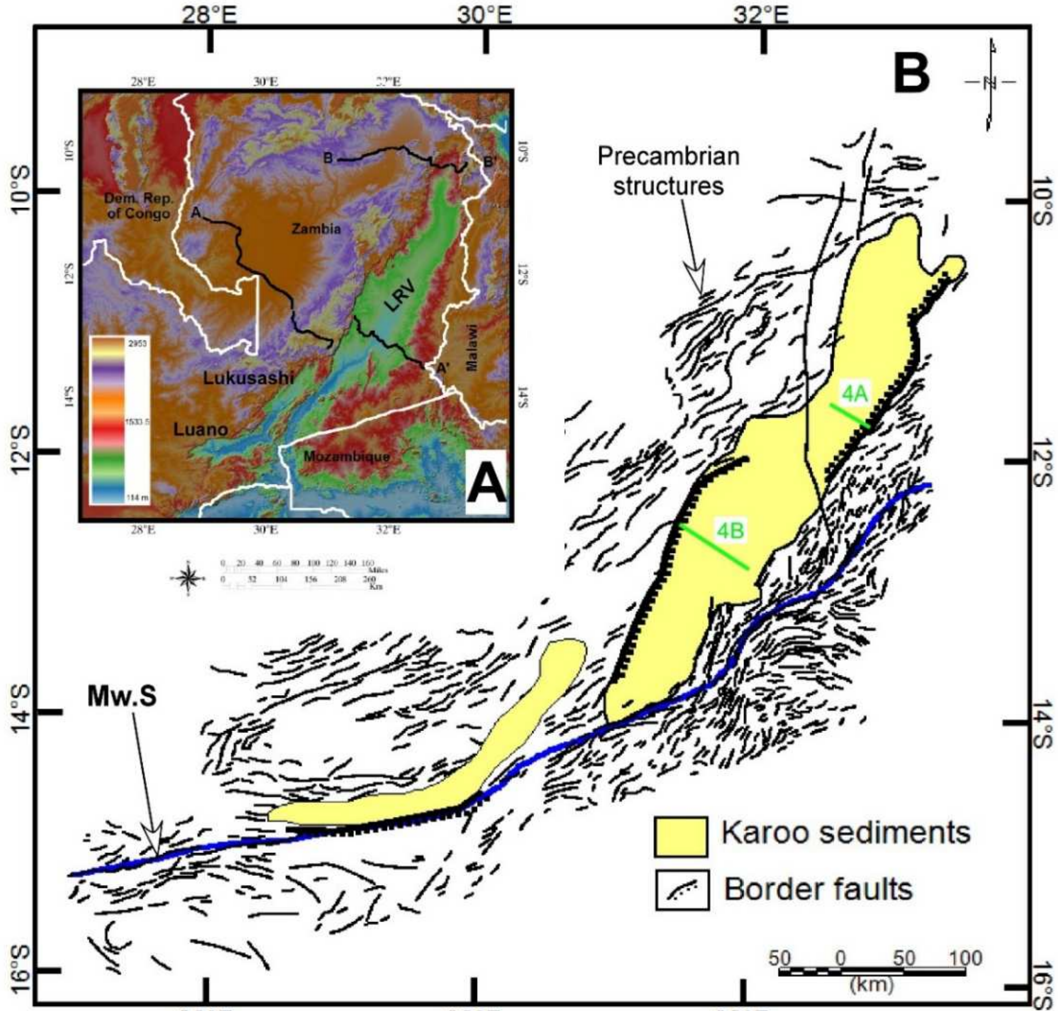

Figure 3: (A) Shuttle Radar Topography Mission (SRTM) Digital Elevation Model (DEM) of eastern Zambia showing the geomorphology of the Luangwa Rift Valley (LRV). A-A' and B-B' profiles show the location of terrestrial gravity data acquired during this study. (B) Structural map of the LRV generated through the interpretation of rift-related structures from SRTM DEM in (A), and through the extraction of the Precambrian structural trends by applying edge detection filters and combining them to produce the ternary image in Fig. 5. Mw.S. is the Mwembeshi shear zone. 4A and 4B are locations of seismic sections shown in Fig. 4.

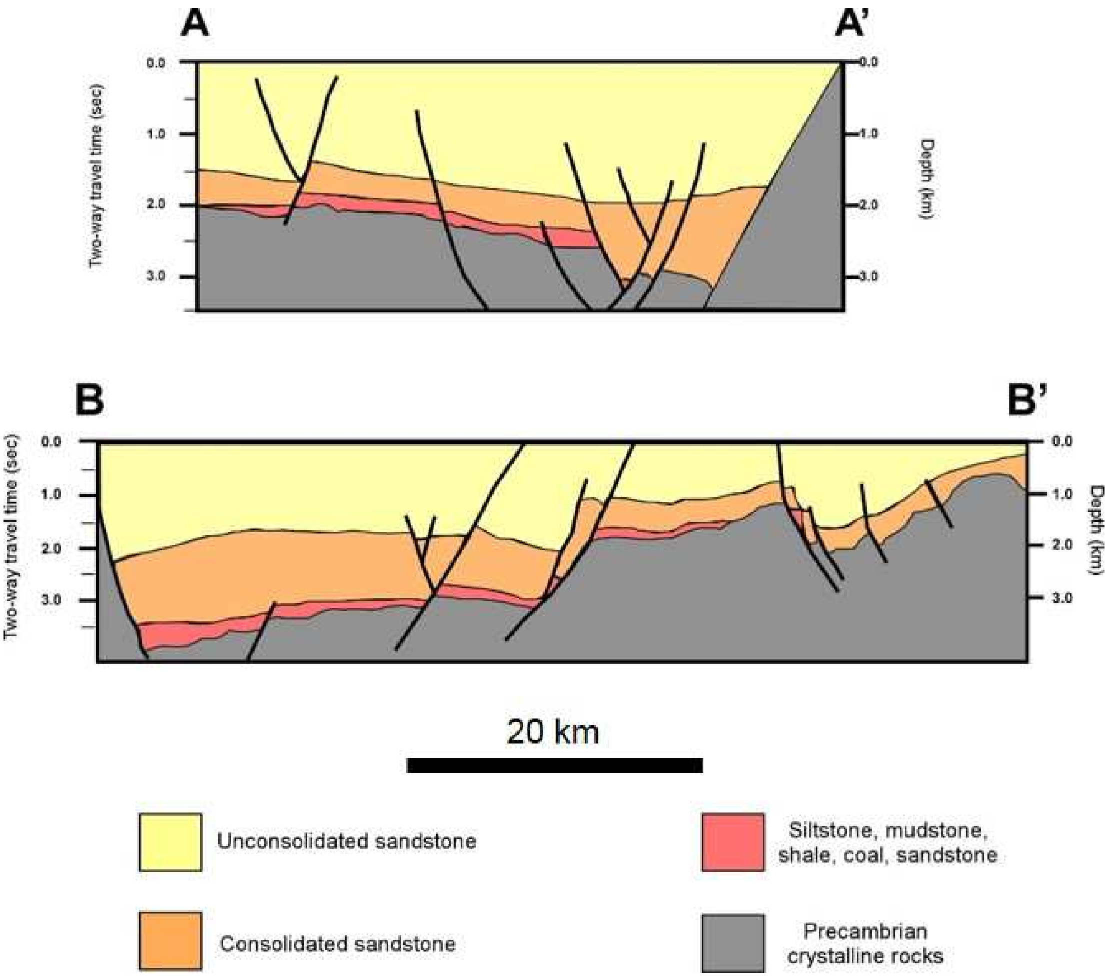

Figure 4: Geological sections interpreted from seismic sections (Banks et al., 1995) across the northern (A) and southern (B) sub-basins of the Luangwa Rift Valley (LRV). See Fig. 3 for location of the profiles.

Characterized by sharp escarpments especially on its northwestern flank, the LRV has been appended to the southwestern branch of the EARS because of possible reactivation of the Karoo normal faults, accompanied by slight subsidence (Delvaux, 1989, Delvaux et al., 1992; Chorowicz, 2005). Utting (1976) reported renewed vertical movements in the northern parts of the LRV. Also observed in the LRV is the occurrence of hot springs along major, deep-seated faults, with the most preferred location being the intersection of fractures and fault systems (Legg, 1974; Sakungo, 1985). Detailed geochemical analyses of the hot spring waters led Legg (1974) and Sakungo (1985) to suggest the origin of the hot springs to be meteoric water percolating along the deep faults and heated by the normal geothermal gradient, dismissing the likelihood of the presence of thermal anomaly at depth beneath the LRV.

CHAPTER III

DATA AND METHODS

Magnetotelluric (MT) and seismic techniques have been traditionally used to estimate crustal thickness and image the thermal structure of the lithosphere, with low electrical resistivities (Whaler and Hautot, 2006) and low seismic wave velocities (e.g., Wolbern et al., 2010; Jakovlev et al., 2011; Mulibo and Nyblade, 2013) providing evidence of thinned crust and possibly elevated heat flow values. The use of these techniques is however, limited in investigating large areas due to their expense and time needed for collecting data. Using power density spectral analysis of aeromagnetic and gravity data to determine the thermal structure of the lithosphere (depth to the Curie isotherm point) and crustal thickness (depth to the Moho) offers an affordable and reliable alternative (e.g., Hussein et al., 2013; Leseane et al., 2015). In addition, the large spatial coverage of potential field data allows the determination of the thermal structure and crustal thickness over wide areas.

3.1 Data sets

3.1.1 Terrestrial-gravity data

Terrestrial gravity data were collected along major roads across the LRV at 2 km station spacing. The locations of the profiles (A-A' and B-B') are shown in Figs. 3A, 5 and 8. The latitude, longitude and ellipsoidal elevations were determined using the differential Global Positioning System (GPS). A geoid correction was applied to the elevation data so the data could be merged with previously collected gravity data in the region. The data set (Appendix 1) was reduced using sea-level as a datum and 2.67 g/cm^3 as the Bouguer reduction density. 2.67 g/cm^3 represents the average density of the continental crust. Moreover, the gravity data were terrain-corrected using the 90 meter Shuttle Radar Topography Mission (SRTM) Digital Elevation Model. The average accuracy of the data is in the order of 0.01 mGal.

3.1.2 Aeromagnetic data

The aeromagnetic data used in this study [Fig. 5] were acquired by the Geological Survey of Zambia at a flight altitude of 150 m and line spacing of 250 m in the north-south direction. The data were provided as a grid with a cell spacing of 5.2 km and 4.4 km in the X and Y directions, respectively. The International Geomagnetic Reference Field (IGRF) was removed from the data.

3.1.3 Satellite gravity data

Satellite gravity data from the World Gravity Map 2012 (WGM12) model [Fig. 8] (Balmino et al., 2012; Bonvalot et al., 2012), with a spatial resolution of about 9 km, was used in this study to estimate the thickness of the crust beneath the LRV and the surrounding regions. The WGM12 model comprises of surface gravity measurements (from land, airborne and marine surveys), and satellite gravimetry (from the GRACE mission) (Bonvalot et al., 2012). Bouguer gravity data were computed using the spherical correction instead of the flat or regular slab correction (Balmino et al., 2012).

A data management plan for all data used in this study is provided in Appendix I.

3.2 Curie Point Depth (CPD) analyses

There are a variety of methods to determine the depth to the base of magnetic sources from the spectral analysis of magnetic data (Spector and Grant, 1970; Bhattacharyya and Leu, 1975; Okubo et al., 1985; Chiozzi et al., 2005; Tanaka and Ishikawa, 2005; Bansal et al., 2011; Manea and Manea, 2011). These can be classified into two broad categories depending on the magnetization models adopted: (1) random magnetization models; and (2) fractal magnetization models. When assuming random magnetization, two methods commonly used: (A) the spectral peak method, proposed originally by Spector and Grant (1970) and subsequently used by researchers such as Shuey et al. (1977); Connard et al. (1983); Ross et al. (2006); Ravat et al. (2007); and (B) the centroid method originally suggested by Bhattacharyya and Leu (1975) and subsequently modified by Okubo et al., (1985) and Tanaka et al., (1999). The spectral peak method determines the position of the observed spectral peak to be a function of the depth to the top (Z_t) and base (Z_b) of the magnetized layer, while the centroid method determines the relationship between the slopes of plots of the power spectrum of the magnetic anomalies against wavenumbers to represent the depths to the base of the magnetized crust. The fractal magnetization model is derived from the concept of self-similarity which is consistent with magnetic susceptibility logs (Salem et al., 2014) and assumes that the magnetization source distribution follows a fractal/scaling distribution (e.g., Pilkington and Todoeschuck, 1990; Maus and Dimri, 1994; Bansal et al., 2011; Bouligand et al., 2009; Salem et al., 2014). This study uses the centroid method because it is relatively easy to implement, while providing reliable Curie Point Depth (CPD) estimates.

In this study the depth to the CPD values were determined on the basis of statistical methods that relate the radially averaged two-dimensional (2D) power spectrum of magnetic anomalies to the basal depth of the magnetized sources (Spector and Grant, 1970; Bhattacharyya and Leu, 1975; Okubo et al., 1985; Chiozzi et al., 2005; Tanaka and Ishikawa, 2005; Bansal et al., 2010; Manea and Manea, 2011; Hussein et al., 2013). Previous studies (e.g., Okubo et al., 1985) showed that by calculating the radially averaged 2D power spectra, the CPD values can be estimated in two steps: (1) Determining the depth to the centroid (Z_o) by plotting (ln[PowerSpectrum/k]) against the wavenumber (k) and calculating the slope of a linear fit at lower wavenumber portions (e.g., 0.08-0.35 rad/km) of the curve; (2) Determining the depth to the top (Z_t) of the magnetized source in a similar fashion by plotting (ln[PowerSpectrum]) against k and calculating the slope at higher wavenumber portions (e.g., 0.5-1.4 rad/km) of the curve. The depth to the base of the magnetized layer (Z_b) is then computed as:

$$Z_b = 2Z_o - Z_t \qquad (1)$$

The aeromagnetic data were divided into sub-regions of 1^o x 1^o (~110km x 110km) that are overlapping by 50% in order to provide more consistent results (Tanaka et al., 1999), and to reduce edge effects due to Gibbs phenomenon that result from the transformation of the spatial aeromagnetic data into the frequency domain using the Fast

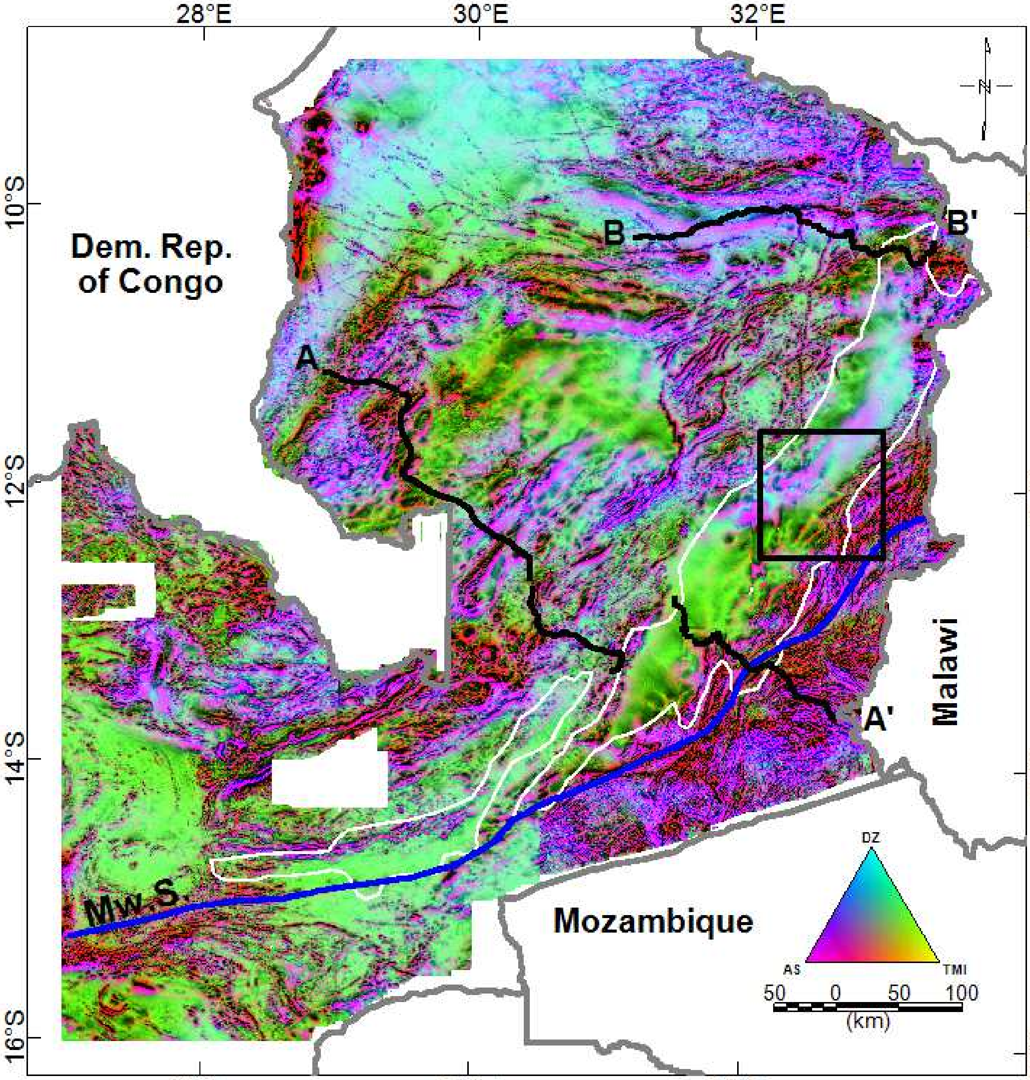

Figure 5: Magnetic ternary image of eastern Zambia produced from a combination of the analytic signal (AS), vertical derivative (DZ) and total magnetic intensity (TMI) in Red-Green-Blue color space. The Luangwa Rift Valley (LRV) is outlined with white lines. A-A' and B-B'

profiles show the location of ground gravity data acquired during this study. The black box represents the location of the 1° x 1° (110km x 100 km) window used for the generation of the two-dimensional (2D) power spectrum curves shown in Fig. 6 to compute the Curie Point Depth (CPD).

Fourier Transform (Tselentis et al., 1988). Fig. 6 shows an example of the power spectral curve for the 1° x 1° sub-region shown in Fig. 5.

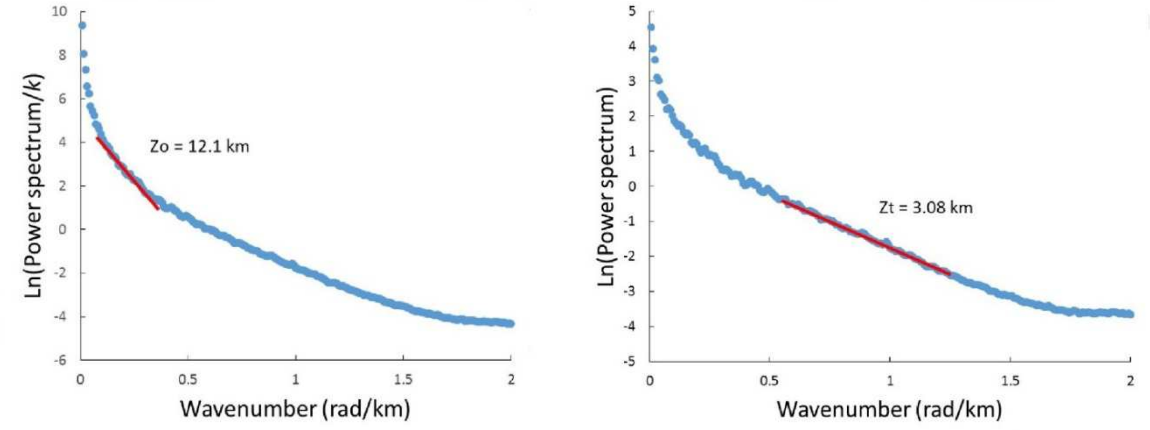

Figure 6: Examples of power-spectrum versus wavenumber curves used to estimate the depth to the centroid (Z_o) and top (Z_t) of the magnetic source for the 1° x 1° (110km x110 km) window shown in Fig. 5.

The adopted centroid method has several limitations. First, the calculated CPD values are representative of the entire 1° x 1° sub-region, and may be an average of shallow and deep CPD values within the sub-region (Hussein et al., 2013). Another limitation is in the uncertainties about the nature of magnetization at depth. It is possible that the calculated CPD values may represent the depth to a lithological contact and not necessarily the depth at which magnetization is lost due to high temperatures (Ross et al., 2006). In spite of these limitations, the centroid method has been successfully used to determine the thermal structure in different regions (e.g., Chiozzi et al., 2005; Tanaka and Ishikawa, 2005; Tanaka et al., 1999; Manea and Manea, 2011). To determine the accuracy of the calculated CPD values, an estimate of the statistical error was computed for each sub-region. The error, as defined by Chiozzi et al. (2005), is the ratio of the standard deviation of the linear fit, to the range of the wavenumber used when determining the gradients for Z_t and Z_o from the spectral curves. The error ranges in this study are found to be from 0.02 to 0.2 km for Z_t, and from 2.1 to 3.3 km for Z_o.

3.3 Heat flow estimates from CPD analyses

Assuming that the temperature gradient is constant between the Earth's surface and the Curie isotherm depth, the one-dimensional heat flow equation (Fourier's Law) is:

$$q = k\,(dT/dz) \qquad (1)$$

where q is heat flux, k is thermal conductivity, T is temperature, z is depth, and dT/dz is temperature gradient.

This equation can be used to estimate the heat flow from the CPD values (Ross et al., 2006; Hussein et al., 2013; Leseane et al., 2015). Tanaka et al. (1999) defined the Curie temperature, C, as:

$$C = (dT/dz)\,D \qquad (2)$$

where D is the CPD value.

Titanomagnetites ($Fe_{3-x}Ti_xO_4$) are a common name for any member of the magnetite ($Fe_3O_4[x=0]$) – ulvospinel ($Fe_2Ti_1O_4[x=1]$) solid solution series, and are the principal carriers of magnetic remanence in nature (Gilder and Le Goff, 2008). Almost all intrinsic physical properties of rocks, such as magnetic susceptibility and Curie temperature, vary with titanium content (Bleil, 1976). Previous studies (e.g. Akimoto, 1962; Syono, 1965; Gilder and Le Goff, 2008) have empirically demonstrated that increasing titanium content in titanomagnetite systematically lowers the spontaneous magnetization and the Curie temperature. The Curie temperature, the temperature at which magnetization is lost, is approximately 580°C (Hunt et al., 1995) for magnetite, the most abundant crustal magnetic mineral.

Assuming that there are no heat flow sources or sinks between the Earth's surface and the CPD values, equation (2) can be modified as:

$$q = (kC)/D \qquad (3)$$

The thermal conductivity, *k*, depends on the geology of the area under investigation. The Precambrian basement rocks of Zambia are dominated by gneisses and schists (Ramsay and Ridgway, 1977; Rainaud et al., 2005) and for this, a thermal conductivity value of 2.96 $Wm^{-1}K^{-1}$ was used in this study. This value is an average of thermal conductivities measured in boreholes in central and eastern Zambia by Chapman and Pollack (1975) and Nyblade and Pollack (1990), and falls within the general range of thermal conductivities (2.5 – 5.0 $Wm^{-1}K^{-1}$) for metamorphic rocks (Lillie, 1999).

3.4 Three-dimensional (3D) inversion

In order to determine the geometry of the magnetized crust within and outside the LRV, the aeromagnetic data [Fig. 5] were divided into 1^{o} x 1^{o} (110 km x 110 km) sub-regions and inverted for three-dimensional (3D) magnetic susceptibility configurations using the algorithm of Li and Oldenburg (1996). Inversion parameters (such as the starting models and the mesh size) were systematically adjusted following the procedures of Hussein et al. (2013) and Leseane et al. (2015). Fig. 7 shows the observed and calculated magnetic anomalies from the 1° x 1° sub-region shown in Fig. 5.

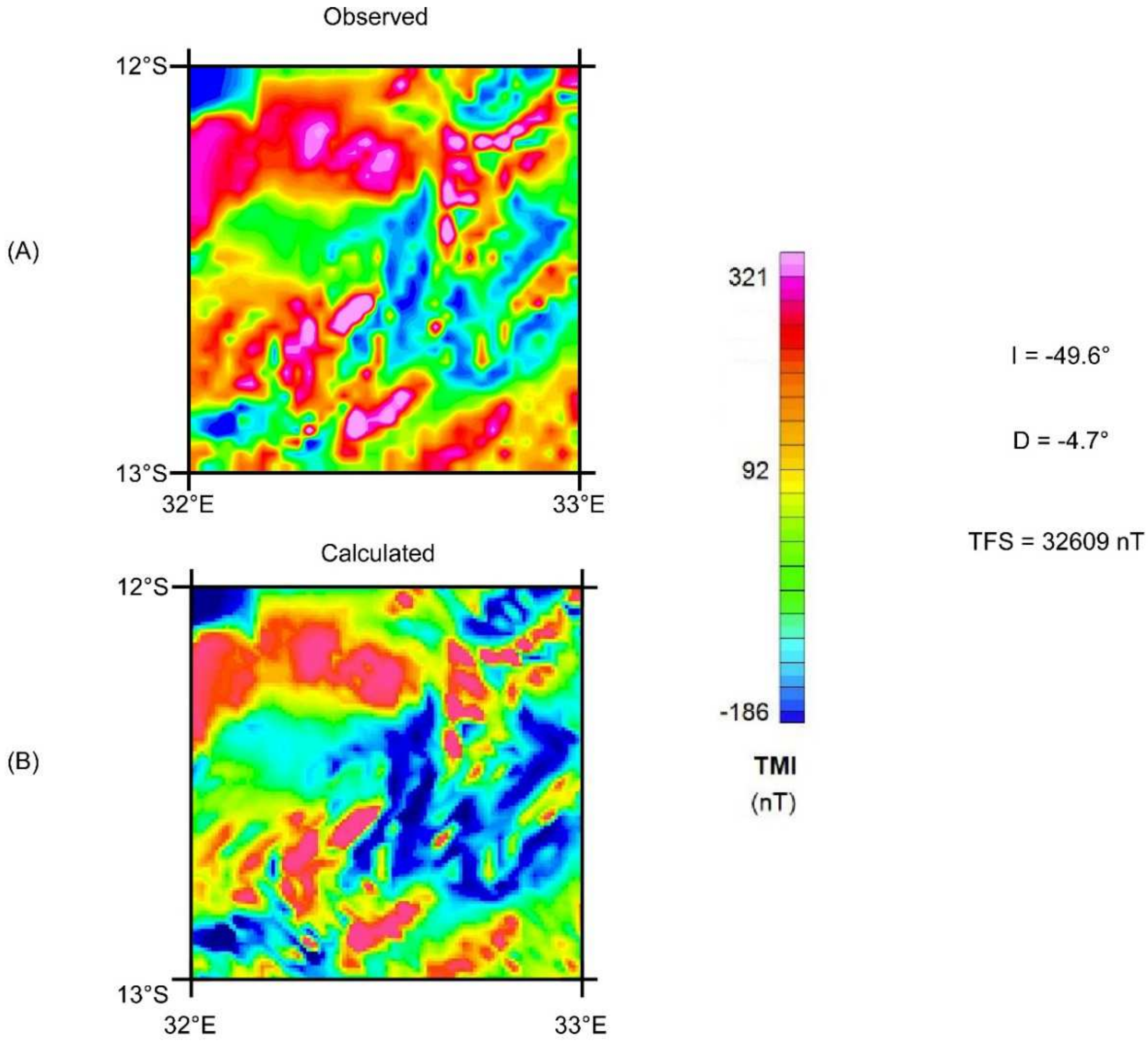

Figure 7: Observed **(A)** and calculated **(B)** magnetic anomalies of the 3D magnetic inversion model of the 1° x 1° (110km x110 km) window shown in Fig. 5. I = inclination. D = declination. TFS = total field strength. TMI = Total Magnetic Intensity.

3.5 Moho depth analyses

The method of Tselentis et al. (1988) was used in estimating the depth to the Moho. The satellite gravity data were upward continued to 2 km to remove the effects of shallow sources, and then divided into 1^o x 1^o (110X110 km) sub-regions with an overlap of 50%. By calculating the 2D radially averaged power spectrum of the gravity data and plotting ln(PowerSpectrum) against the wavenumber (*k*), Tselentis et al. (1988) showed that the depth to the causative bodies can be estimated by fitting straight lines through the linear segments of the curve.

An example of a power spectral curve is shown in Fig. 9 for the 1^o x 1^o sub-region shown in Fig. 8. Three linear segments were identified on almost all the power spectral curves. These segments represent different density discontinuities (Fairhead and Okereke, 1987; Tselentis e al., 1988; Gomez-Ortiz et al., 2005). The highest wavenumber segment represents the regional or deep causative bodies while the lowest wavenumber portion corresponds to shallow causative bodies or random noise contained in the data. The intermediate slopes (corresponding to the intermediate wavenumber segment (0.1-0.37 rad/km)) represent the Moho depth (Tselentis et al., 1988; Sanchez-Rojas and Palma, 2014). The error in the Moho depths estimates was calculated as the standard deviation of the linear fit of the intermediate segment. The error estimates range from 0.7 to 2.9 km.

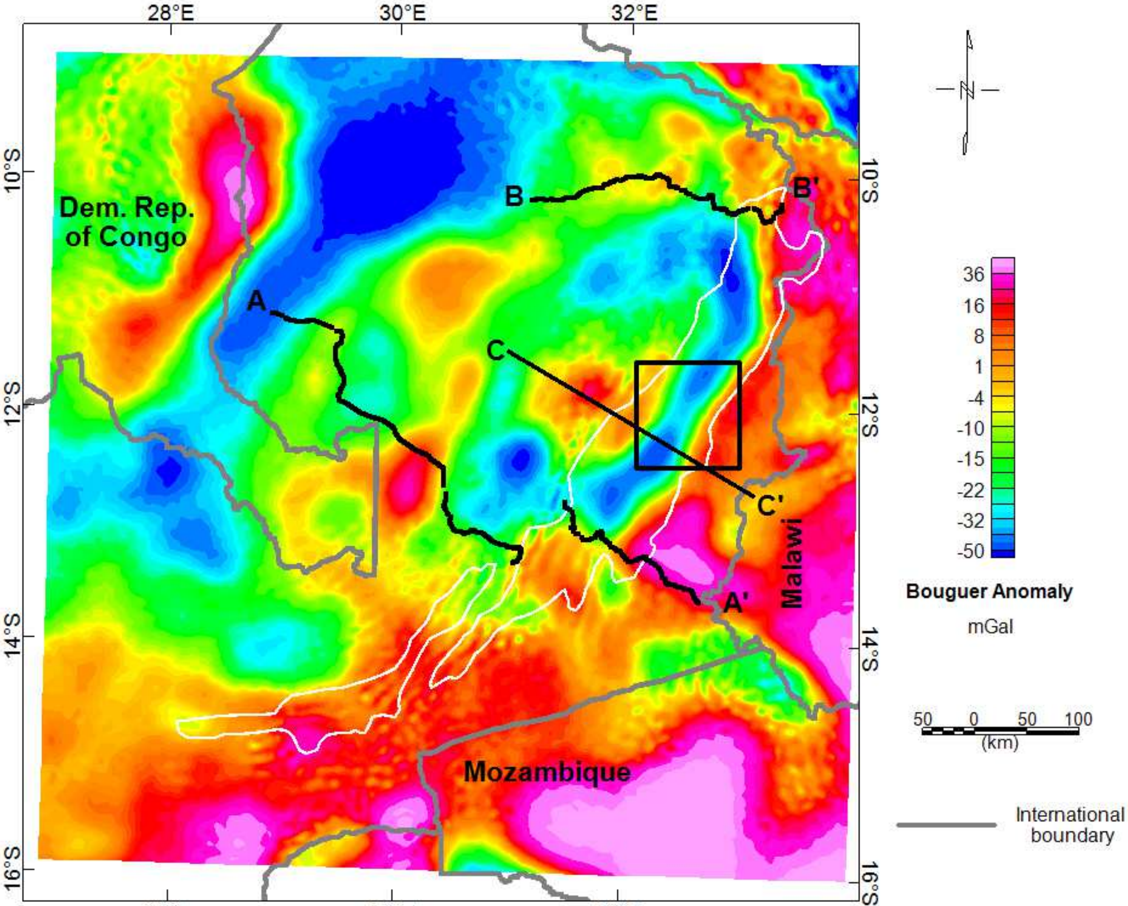

Figure 8: Satellite Bouguer anomaly map extracted from the World Gravity Map 2012 (WGM 2012) used for estimating the crustal thickness beneath the Luangwa Rift Valley (LRV) and surroundings using 2D power-density spectrum analysis. The LRV is outlined white lines. A-A' and B-B' profiles show the location of ground gravity data acquired during this study. The black box represents the location of the 1° x 1° (110km x110 km) window used for the generation of the power spectrum curve shown in Fig. 9 for computation of the crustal thickness.

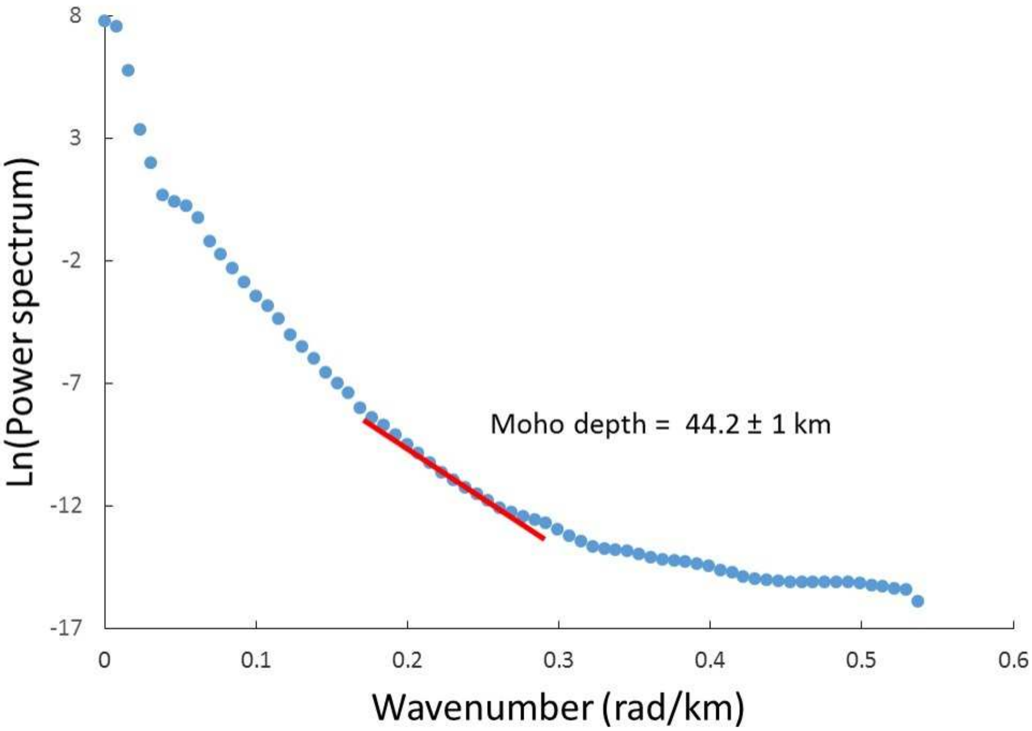

Figure 9: An example of the 2D power-density spectrum curve used to estimate the crustal thickness for the 1º x 1º (110km x110 km) window shown in Fig. 8.

CHAPTER IV

RESULTS

4.1 Curie point depth and heat flow

The CPD values in eastern Zambia range from 20 to 35 km [Fig. 10], while the heat flow values range from 46 to 78 mW/m^2 [Fig. 11]. The shallowest CPD values (≤ 24 km), coupled with high heat flow values (> 70 mW/m^2) occur beneath the Mporokoso basin and some parts of northwest Irumide belt. Beneath the LRV, shallow CPDs occur in the northern-most tip, some areas in the central part of the rift, and also at the overlap zone between the LRV and the Lukusashi rift. A north-south trend of deep CPD values (>24 km) and low heat flow (~59 to 64 mW/m^2) extends from northern Zambia into the central part of the LRV. Deep CPD values and low heat flow anomalies are also observed at the southwestern-most tip of the rift in west-central Zambia, and north of the rift segmentation point.

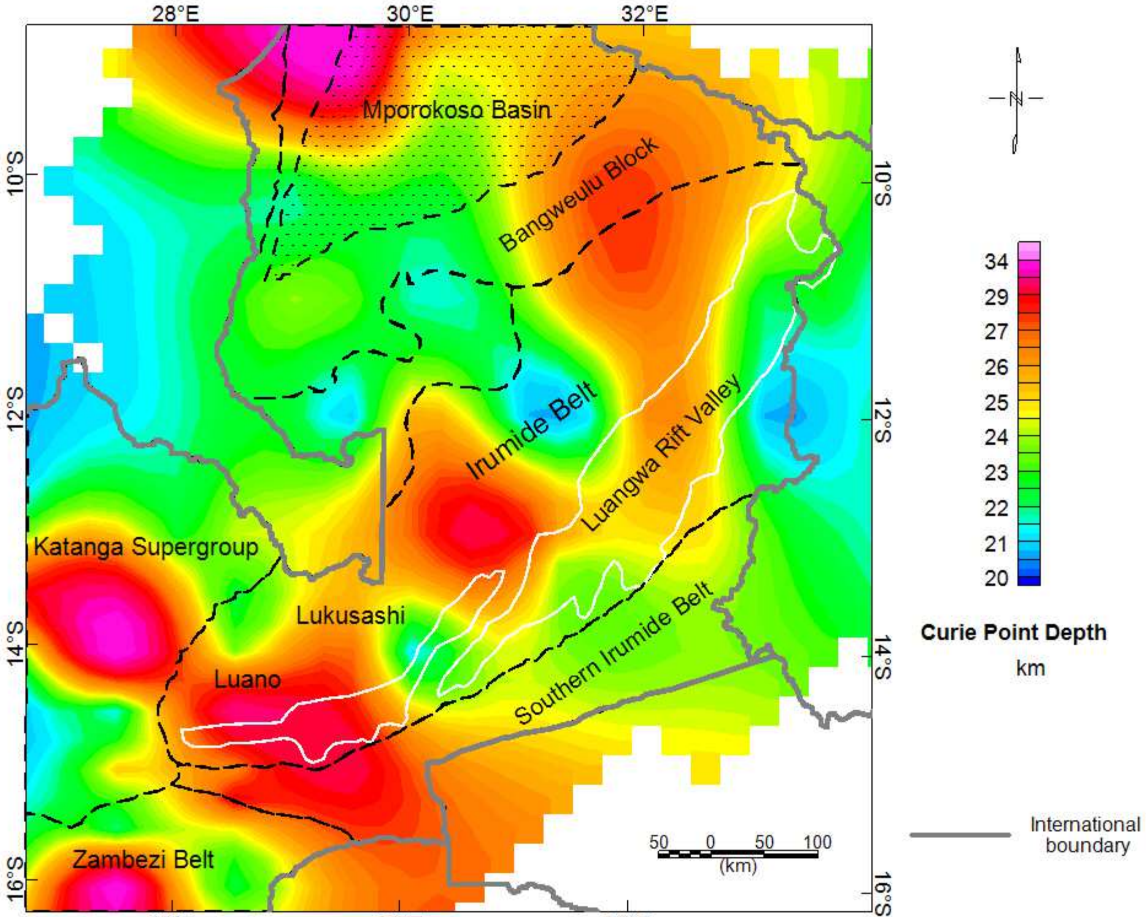

Figure 10: Map of the Curie Point Depth (CPD) values beneath the Luangwa Rift Valley (LRV) and surroundings obtained from 2D power-density spectrum analysis of the aeromagnetic data in Fig. 5. The LRV is outlined with white lines. Tectonic elements from Fig. 2 (B) are outlined with dashed lines.

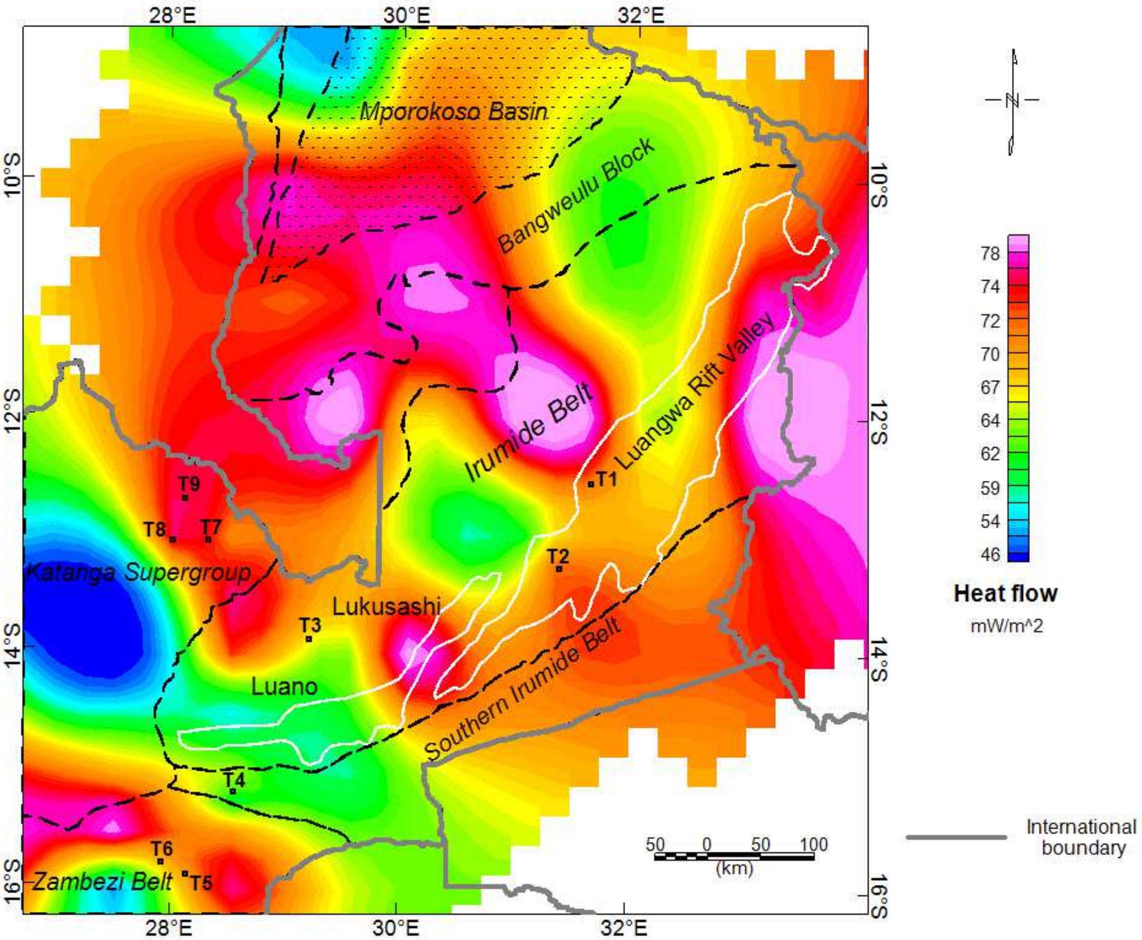

Figure 11: Map of the heat flow beneath the Luangwa Rift Valley (LRV) and surroundings calculated from the Curie Point Depth (CPD) values which are obtained from the 2D power-density spectrum analysis of aeromagnetic data in Fig. 5. The LRV is outlined with white lines. Tectonic elements from Fig. 2 (B) are outlined with dotted lines. The black dots labeled T1-T9 show locations of borehole-measured heat flow values by Chapman and Pollack (1975).

4.2 Moho depths

The Moho depth estimates range from 29 to 55 km [Fig. 12]. The shallowest Moho depths (29 to 38 km) occur beneath the Mporokoso basin and west-central Zambia.

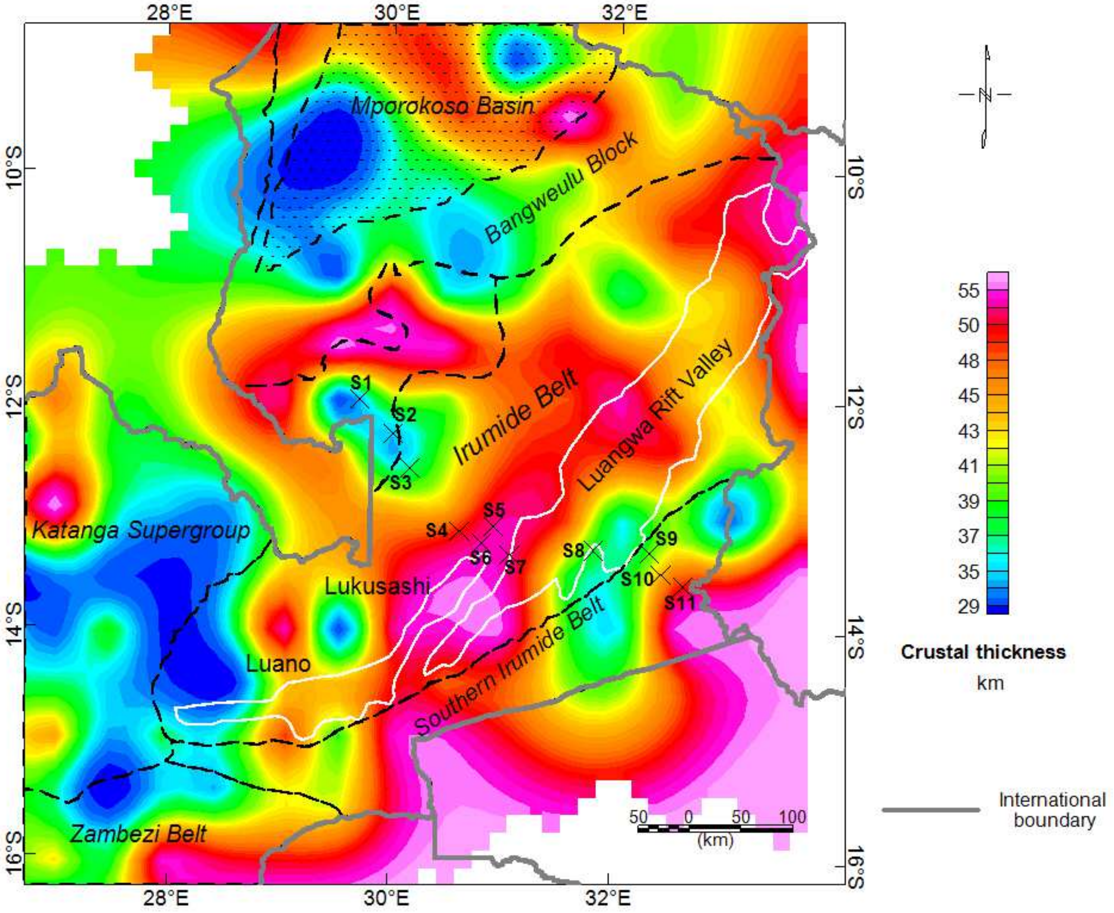

Figure 12: Map of the crustal thickness below the Luangwa Rift Valley (LRV) and surroundings obtained from the 2D power-density spectrum analysis of the satellite gravity data in Fig. 8. The LRV is outlined with white lines. Tectonic elements from Fig. 2 (B) are outlined with dotted lines. The black crosses labeled S1-S11 show locations of passive seismic stations (Yu et al., 2013).

The southwestern-most tip of the LRV extends within the anomalously shallow Moho depth area. The thickest crust (>40 km) occurs at localized areas in northwestern and northern Zambia, and beneath the Irumide belt. With the exception of localized regions of shallow Moho depths (35 to 39 km) occurring in the southeastern part of central LRV, deep Moho depths (>40 km) underlie much of the rift, especially beneath its northwestern flank. The deepest crustal thickness (~55 km) is found beneath the overlap zone between the LRV and the Lukusashi rift. The anomalously shallow Moho depths over the Mporokoso Basin and in west-central Zambia are beyond the scope of this study.

In order to test the consistency of the Moho depth results obtained along the entire length of the LRV and surroundings from the 2D power spectrum of satellite gravity data using 50% overlap of sub-regions, the data were analyzed for the second time using even higher (90%) overlapping, and the results were in agreement (within 1 to 3 km) with those from our standard overlap of 55^0.

4.3 Three-dimensional (3D) inversion

Fig. 13 shows the 3D inversion model cube of the aeromagnetic data over the sub-region shown in Fig. 5. Due to the lack of constraints in the LRV, a range of magnetic susceptibility from 0-0.03 SI was adopted from the study of the Okavango rift zone (Leseane et al., 2015). Several adjacent inversion cubes were overlapped side-by-side to produce a continuous 2D profile. An example of such a 2D profile along A-A’ is shown in Fig. 14, with thick magnetized blocks beneath the LRV extending to about 30-40 km depth.

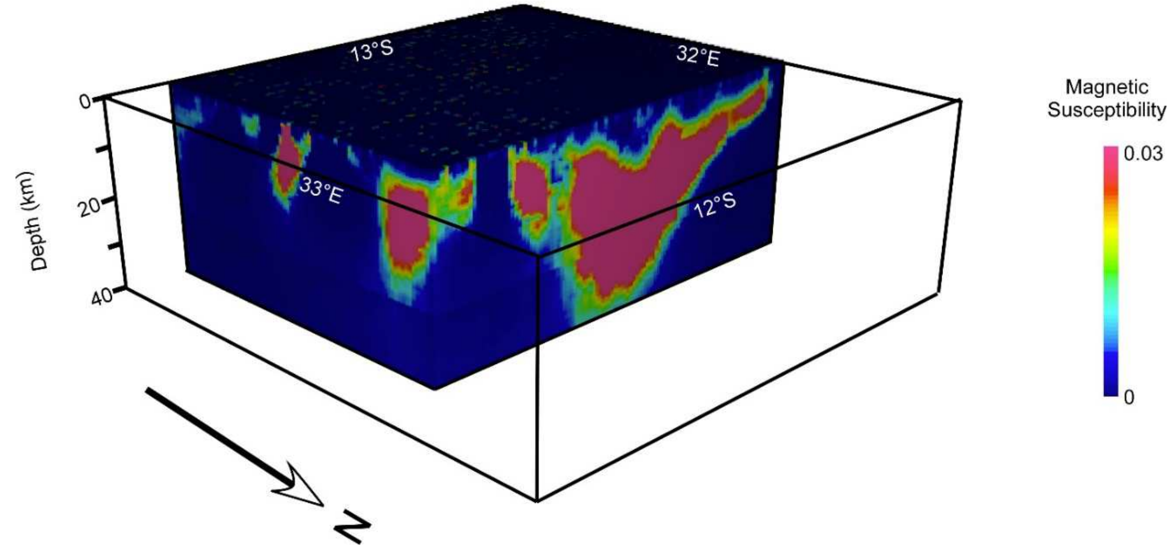

Figure 13: 3D inversion cube of the aeromagnetic data over the 1º x 1º (110km x110 km) window shown in Fig. 5.

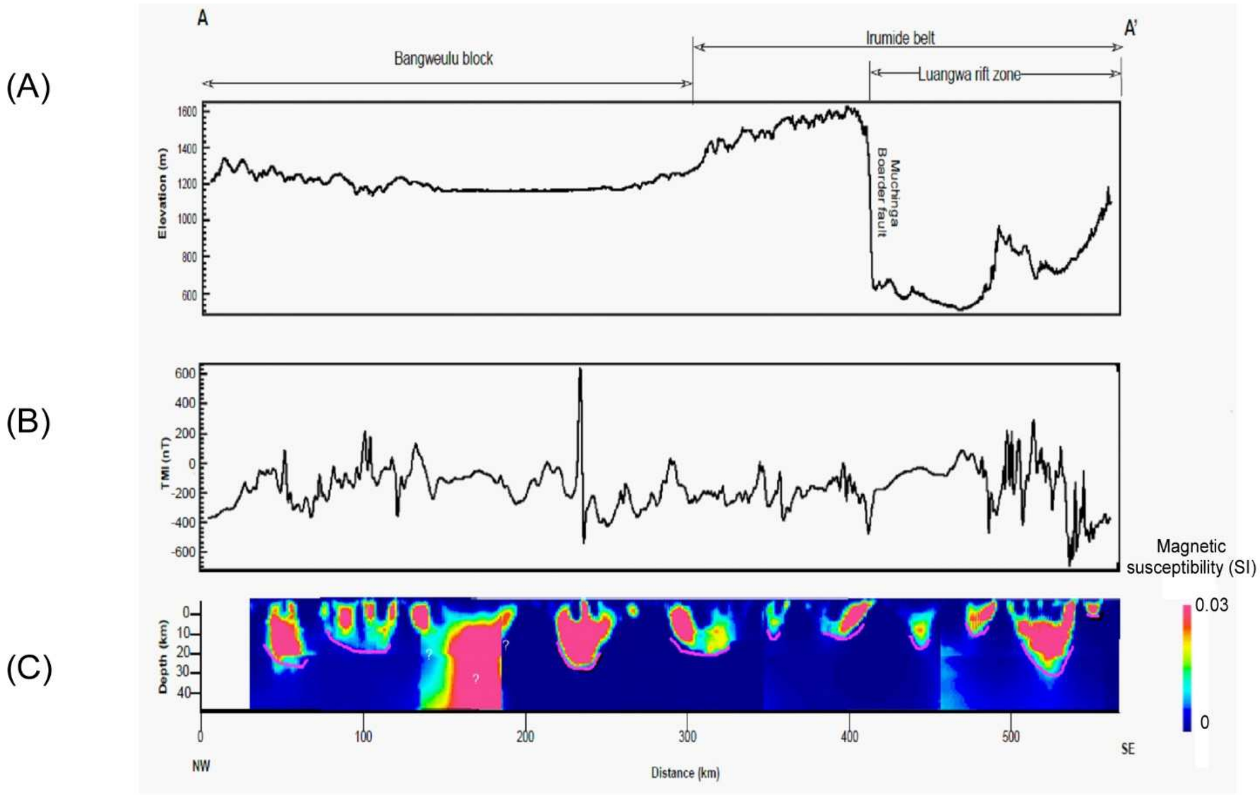

Figure 14: (A) Topography extracted from Shuttle Radar Topography Mission (SRTM) Digital Elevation Model (DEM). (B) Variation of total magnetic intensity (TMI). (C) Results of 3D inversion of aeromagnetic data shown in Fig. 5 along profile A-A' showing thick magnetic bodies beneath and outside the Luangwa Rift Valley (LRV). See Fig. 5 for location of the profile.

CHAPTER V

DISCUSSION

5.1 Thermal structure beneath the LRV

Results of this study suggest that there is no systematic correlation between the elevated CPD values and heat flow values on one hand and the geographic extent of the rift. The CPD values range from 22 to 27 km within the rift as well as immediately outside the rift. The corresponding heat flow for the same areas ranges from 62 to 74 mW/m^2. Taking the average geothermal gradient for the Precambrian basement rocks in Zambia to be ~23 ^oC/km (Legg, 1974), and assuming a Curie temperature of 580 ^oC, the normal CPD value is expected to be around 25 km (580 ^oC/23 ^oC km^{-1}). The LRV and surrounding areas therefore exhibit normal CPD values.

Nyblade and Pollack (1993) estimated the average heat flow within orogenic belts to be between 60 and 70 mW/m^2. The calculated heat flow in this study therefore shows that the Irumide belt has a normal thermal structure typical of orogenic belts. As shown in Table 1, the heat flow estimates of this study are comparable to heat flow values measured in boreholes [Fig. 11] by Chapman and Pollack (1975) and Nyblade and Pollack (1990).

Table 1. Comparison between the heat flow values calculated from the Curie Point Depth (CPD) values and those determined from borehole measurement by Chapman and Pollack (1975), and Nyblade and Pollack (1990)

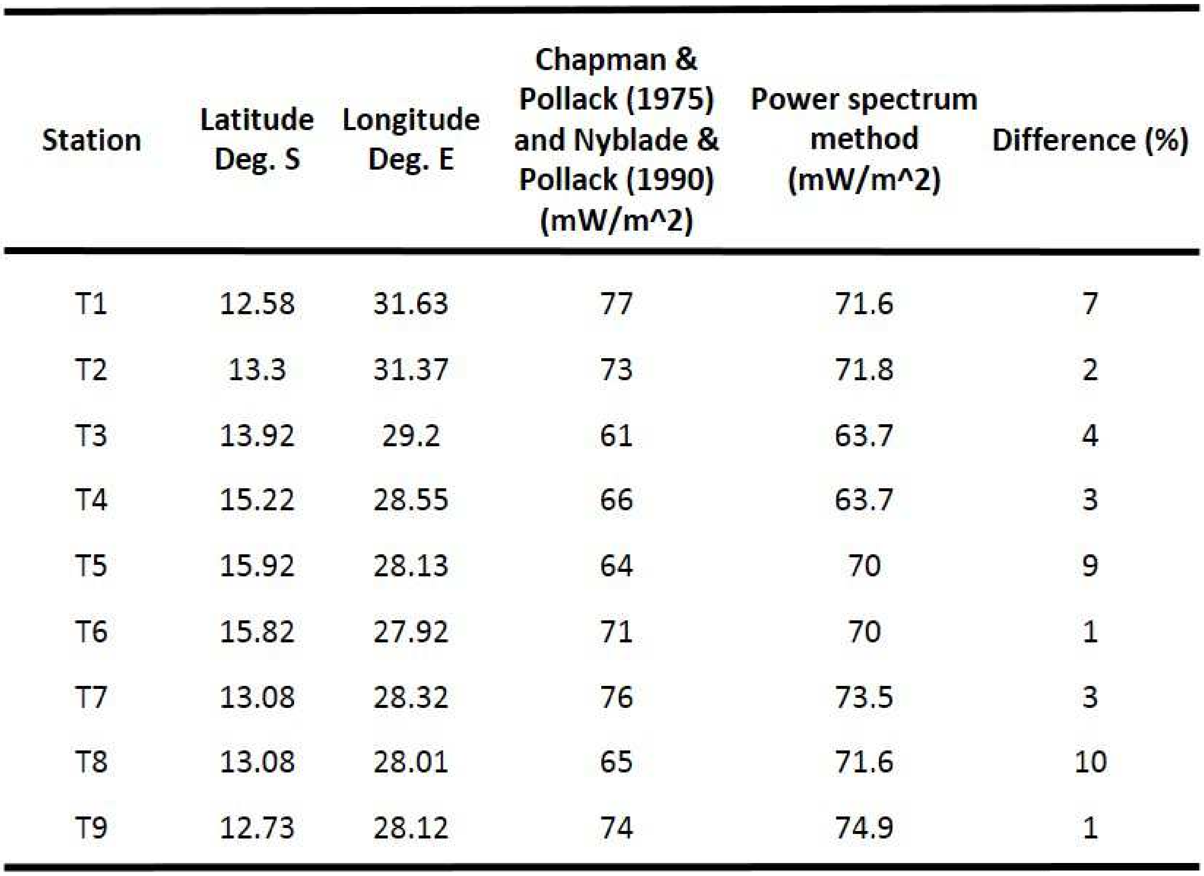

Station	Latitude Deg. S	Longitude Deg. E	Chapman & Pollack (1975) and Nyblade & Pollack (1990) (mW/m^2)	Power spectrum method (mW/m^2)	Difference (%)
T1	12.58	31.63	77	71.6	7
T2	13.3	31.37	73	71.8	2
T3	13.92	29.2	61	63.7	4
T4	15.22	28.55	66	63.7	3
T5	15.92	28.13	64	70	9
T6	15.82	27.92	71	70	1
T7	13.08	28.32	76	73.5	3
T8	13.08	28.01	65	71.6	10
T9	12.73	28.12	74	74.9	1

These results demonstrate the lack of a thermal anomaly or accentuated geothermal gradient beneath the LRV.

The absence of a thermal anomaly is corroborated by geochemical analyses of hot springs within and around the rift valley. These analyses did not demonstrate any geochemical signature indicative of interaction of surface water with a deep heat source such as magma (Legg, 1974; Sakungo, 1985). Legg (1974) and Sakungo (1985) postulated the origin of the hot springs to be meteoric waters percolating to great depths down into dilatational faults and these are being heated by the normal geothermal gradient. It is unlikely that these hot springs are associated with magmatic activities because the last known volcanic activity in Zambia is thought to have occurred during the Karoo rifting event, 180 Ma ago (Sakungo, 1985). The presence of mantle transition zone at normal depth (~410-660 km) beneath the LRV also supports the absence of a thermal anomaly (Yu et al., 2014). The high heat flow observed over the Mporokoso Basin is attributed to the thin crust [Fig. 12] and uranium mineralization occurring within the basin (e.g., *Andrews-Speed*, 1986; 1989; *De Waele and Fitzsimons*, 2007).

5.2 Crustal structure beneath the LRV

Results of this study showed that the Moho is deeper (~50 km) under the entire LRV especially on its north-western flank. It is not unusual to observe such thicker continental crust beneath rift systems. For example, the crustal thickness beneath the Baikal rift varies from 35 to 55 km, with localized thinning (35 to 40 km) observed beneath the rift basins and 45 to 55 km thick crust observed beneath major horst blocks (Logatchev and Zorin, 1992). Also, beneath the 1.1 Ga North American Midcontinent rift, crustal thickness of up to 55 km have been imaged by seismic studies (e.g., Halls, 1982; Behrendt et al., 1990; Trehu et al., 1991; Hinze et al., 1992;

Shay and Trehu, 1993). In both cases, the thick crusts beneath the rifts have been attributed to magmatic under-plated bodies. The LRV basin does not show any evidence of a thinned crust except towards its south-eastern part where the Moho depths range from 35 to 39 km. Outside the rift basin, shallower Moho depths (35 to 45 km) are observed.

Comparison between the Moho depths estimations of this study from gravity data and those obtained from preliminary results of a passive seismic study [Fig. 12] along profile A-A' (Yu et al, 2013) is provided in Table 2. Away from the rift, the gravity-derived Moho depths are comparable with those determined from the passive seismic study. However, closer to the rift itself, the Moho depths estimations from the two methods differ by up to 12.9 km, with the gravity analysis giving deeper Moho compared to the passive seismic analysis. The 10 to 12 km difference in crustal thickness from gravity and passive seismic studies may be due to the presence of a thick layer of an under-plated mafic body.

Table 2. Crustal thickness estimated from 2D power-density spectrum analysis of gravity compared with the crustal thickness from passive seismic stations across Luangwa Rift Valley (LRV) (Yu et al., 2014)

Station	Latitude Deg. S	Longitude Deg. E	Seismic-Moho Depth (km)	Gravity-Moho Depth (km)	Difference (%)
S1	12	29.7	34	34.3	0.9
S2	12.3	30	36	34.2	5
S3	12.6	30.15	39.5	36.6	7
S4	13.15	30.6	38.5	49.5	29
S5	12.95	30.4	42	52.2	24
S6	13.25	30.8	39.5	52.4	33
S7	13.35	31.05	41	52	27
S8	13.3	31.8	42.5	38.5	9
S9	13.32	32.3	43	40.1	7
S10	13.5	32.4	43	44.3	3
S11	13.6	32.6	43	49.3	15

5.3 Under-plated Mafic Bodies (UPMBs)

The formation process of UPMBs is poorly understood, but is thought to be due to ascending mafic magma from the mantle which experiences neutral buoyancy and as a result ponds at the Moho (e.g., Fyfe, 1978, 1992; Yamasaki and Gernigoc, 2009; Thybo and Artemieva, 2013). The UPMBs are characterized by high P- and S-wave velocities, high Vp/Vs ratios, and high densities, making seismic and gravity studies the most suitable and most applied techniques in their study (Furlong and Fountain, 1986; Gladczenko et al., 1997; Mjelde et al., 1997; Raum et al., 2002; Thybo and Nielsen, 2009; Yamasaki and Gernigon, 2009; Thybo and Artemieva, 2013). They occur under a wide variety of tectonic settings such as large igneous provinces, contractional regimes, and continental rifts Thybo and Artemieva, 2013). Examples of continental rifts where UPMBs have been imaged include the Baikal rift (e.g., Thybo and Nielsen, 2009), southern Kenya rift (e.g., Hay et al., 1995; Birt et al., 1997; Mechie et al., 1997; Thybo et al., 2000), Main Ethiopian Rift (e.g., Ebinger and Sleep, 1998; Mackenzie et al., 2005; Tiberi et al., 2005), and the North American Midcontinent rift (e.g., Behrendt et al., 1990; Hinze et al., 1992; Shay and Trehu, 1993).

The UPMBs may play a significant role in the evolution and modification of the continental lithosphere (e.g. Furlong and Fountain, 1986; Fyfe, 1978, 1992; Cox, 1980; Thybo and Artemieva, 2013). Crustal heating caused by the under-plating, for example, may cause crustal melting, hence the generation of granitic magma that may solidify to form a granitic crust (e. g., Douce, 1999; Huppert and Sparks, 1988; Coldwell et al., 2011). Yamasaki and Gernigon (2009) have suggested that the UPMBs introduce a rheological heterogeneity that plays an important role in strain localization during the onset of rifting. The rheological heterogeneity brought about by the UPMB is due to two main physical effects: (1) anomalously high temperatures of the UPMB which results in thermal weakening of the crust; and (2) the UPMB's mafic composition which is notably weaker than the mantle (Yamasaki and Gernigon, 2009). In the Basin and Range Province of the western United States, Lachenbruch and Sass (1978) proposed that active under-plating may be a contributing factor to the elevated heat flow in the region. Depending on the size and time-scale of the formation of the UPMB, the temperature anomaly due to the UPMB may disappear within a few million years, so that the rheological heterogeneity due to the difference in composition between the UPMB and the mantle plays a significant role in the localization of strain at any stage of extension (Yamasaki and Gernigon, 2009).

5.4 Gravity forward modeling

This study used 2D forward modeling of ground gravity data to test the possibility of the presence of UPMB beneath the LRV. The gravity profile along profile A-A’ exhibits a broad long-wavelength positive anomaly possibly related to deep dense material beneath the rift. This anomaly is partly superimposed by shorter wavelength positive and negative anomalies at the rift shoulders and floor. The local negative short-wavelength anomalies are attributed to the less-dense rift sediments infill. This interpretation is similar to that of gravity profiles across the North American Midcontinental rift where gravity maxima have been attributed to a thickened continental crust and the presence of mafic intrusive rocks beneath the rift, while gravity minima have been interpreted as due to low density sedimentary rocks [*Hinze et al.*, 1992 *and references therein*; *Shay and Trehu*, 1993].

We subsequently developed 2D forward models of the gravity data along profiles A-A’, B-B’ and C-C’ [Fig. 8] to reconcile the observed thermal and lithospheric structure of the LRV. Gravity models suffer from non-uniqueness and in order to construct meaningful geological models constraints such as lateral and vertical variations of rock units must be used. Because these constraints are not readily available in the LRV and surrounding areas, the crustal thickness estimations obtained from the spectral analysis of satellite gravity data and from preliminary results of the passive seismic study were used as initial constraints in the 2D forward model. Better established constraints for the younger EARS rifts were adopted for the Karoo rifts because of the similar underlying Precambrian structures beneath the two rift systems. The thickness and densities of the upper (2.76 m/cm^3) and lower crust (2.86 and 2.92 g/cm^3) for example, were estimated from gravity and seismic studies of different parts of the EARS (e.g., Mahatsente et al., 1999; Mickus et al., 2007; Leseane et al., 2015). The magnetized bodies from the 3D inversion [Fig. 14] are modeled with a density of 2.95 g/cm^3. The magnetic bodies beneath the LRV are interpreted as mafic intrusions related to the magmatism that emplaced the under-plated mafic body, while the bodies outside the rift are interpreted as dense bodies that pre-date rifting and possibly Precambrian in origin. Upper crustal bodies of various dimensions and densities were introduced in the model to account for lithological variations in the Irumide belt as indicated by geological studies [e.g., *De Waele et al*., 2006].

The 2D forward model along profile A-A' suggests that the Moho is deeper beneath the LRV, and this is due to the presence of an UPMB [Fig. 15]. The apparent difference in crustal thickness obtained from the gravity and passive seismic studies may be because the passive seismic data imaged the Moho as the top of the UPMB whereas the gravity data considered the base of the UPMB as the Moho. It is not uncommon to encounter a discrepancy between seismic and gravity Moho estimates (Mjelde e al., 2013). At the Ontong Java Plateau, a large igneous province located north of Australia, gravity and seismic refraction crustal thickness estimates yield a difference of about 18 km (Gladczenko et al., 1997). Distinguishing between the seismic and petrological Moho, Mengel and Kern (1992) defined the seismic Moho as the first-order velocity discontinuity, and the petrological Moho as the boundary between non-peridotitic rocks of the lower crust and the olivine-dominated sub-continental lithospheric mantle. A similar interpretation is adopted in the current study to explain the difference between the gravity and seismic Moho depths beneath the LRV. It is likely that the passive seismic study was able to effectively image the top of the UPMB because of the large difference in seismic velocity (from 6.6 to 7.4 km/s^2) typically encountered across the lower crust-UPMB boundary (e.g., Mjelde et al., 1997; Raum et al., 2002; Mackenzie et al., 2005; Thybo and Atermieva, 2013). The gravity data on the other hand may have imaged the Moho as the lower boundary between the UPMB and the sub-continental lithospheric mantle because of density difference between the two layers.

The presence of an UPMB below the LRV is further supported by results of the passive seismic study where high Vp/Vs ratios (>1.75) beneath the rift are interpreted as ancient/ongoing magmatic emplacement (Yu et al., 2014). However, the exact timing of UPMB emplacement is difficult to estimate (Yamasaki and Gernigon, 2009). It is possible that the UPMB below the LRV was emplaced before the onset of rifting and may have played a critical role in localizing extension. It is also possible that the magmatic intrusions imaged by the 3D inversion of the aeromagnetic data beneath the rift were emplaced at the same time as the UPMB from a common magmatic source. The feeder dikes between the UPMB and the mafic intrusions were not introduced in the 2D forward model in Fig. 15 because their dimension is too small to be resolved by the gravity data. The fact that this study does not show thermal perturbations beneath the LRV suggests that the temperature anomaly due to the UPMB emplacement has cooled over the 180 Ma since the initiation of rifting.

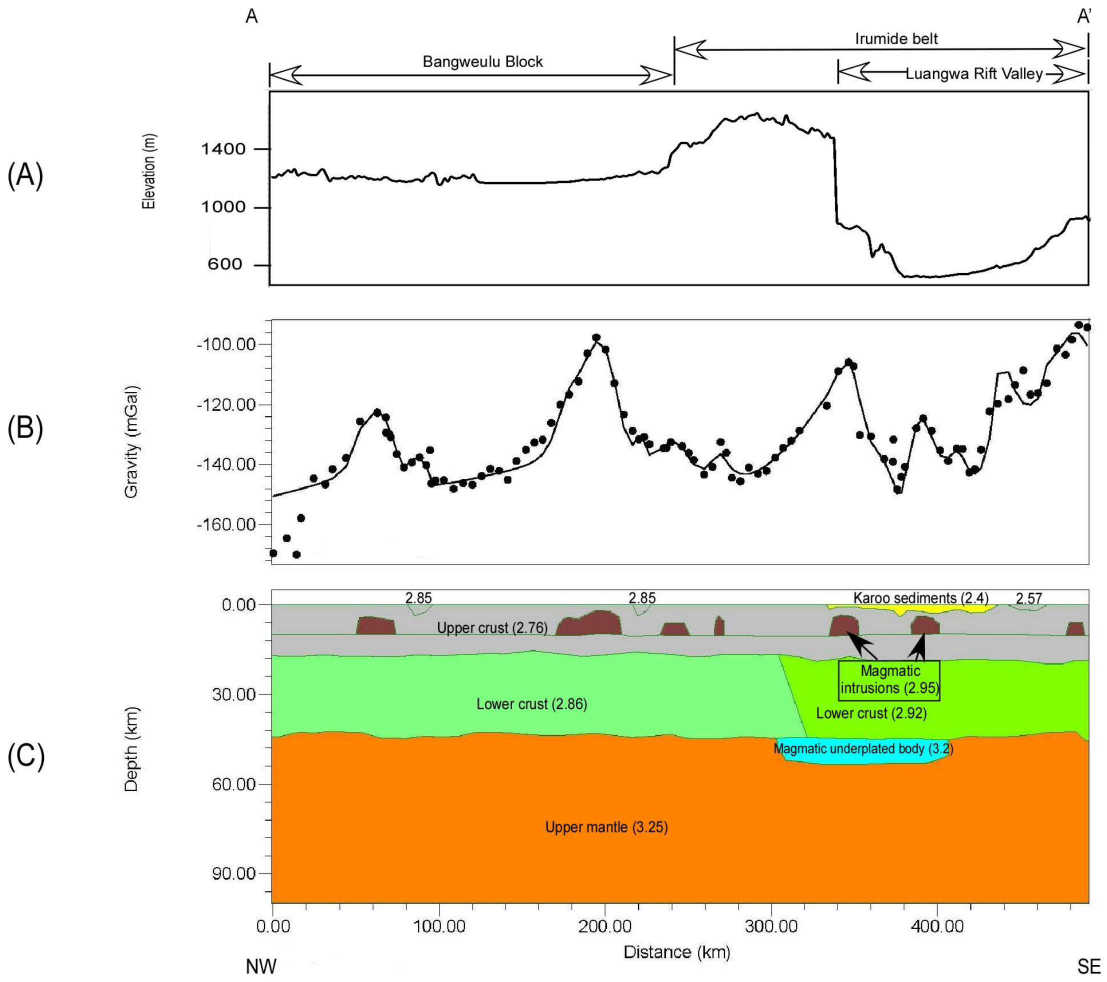

Figure 15: (A) Elevation data collected during this study. (B) Observed (dotted line) Bouguer gravity anomalies across the Luangwa Rift Valley (LRV) along profile A-A' and calculated (solid line) Bouguer gravity anomalies of the two-dimensional (2D) forward model in Fig. 15C. (C) A 2D gravity forward model showing the under-plated mafic body (UPMB) below the LRV. Numbers are densities in g/cm^3. See Fig. 5 for location of the profile.

The lateral extent of the UPMB is not exactly known and additional studies (e.g., passive or active source seismic studies) may be used to delineate its extent beneath the LRV. Two additional profiles (B-B' and C-C' in Fig. 8) were also modeled [Figs. 16 and 17] to examine the lateral extent of the UPMB. The Bouguer gravity anomalies along these profiles do not show a broad-wavelength positive anomaly similar to the one observed along profile A-A' and because of this the models only show a thick crust under the UPMB but without the presence of UPMB.

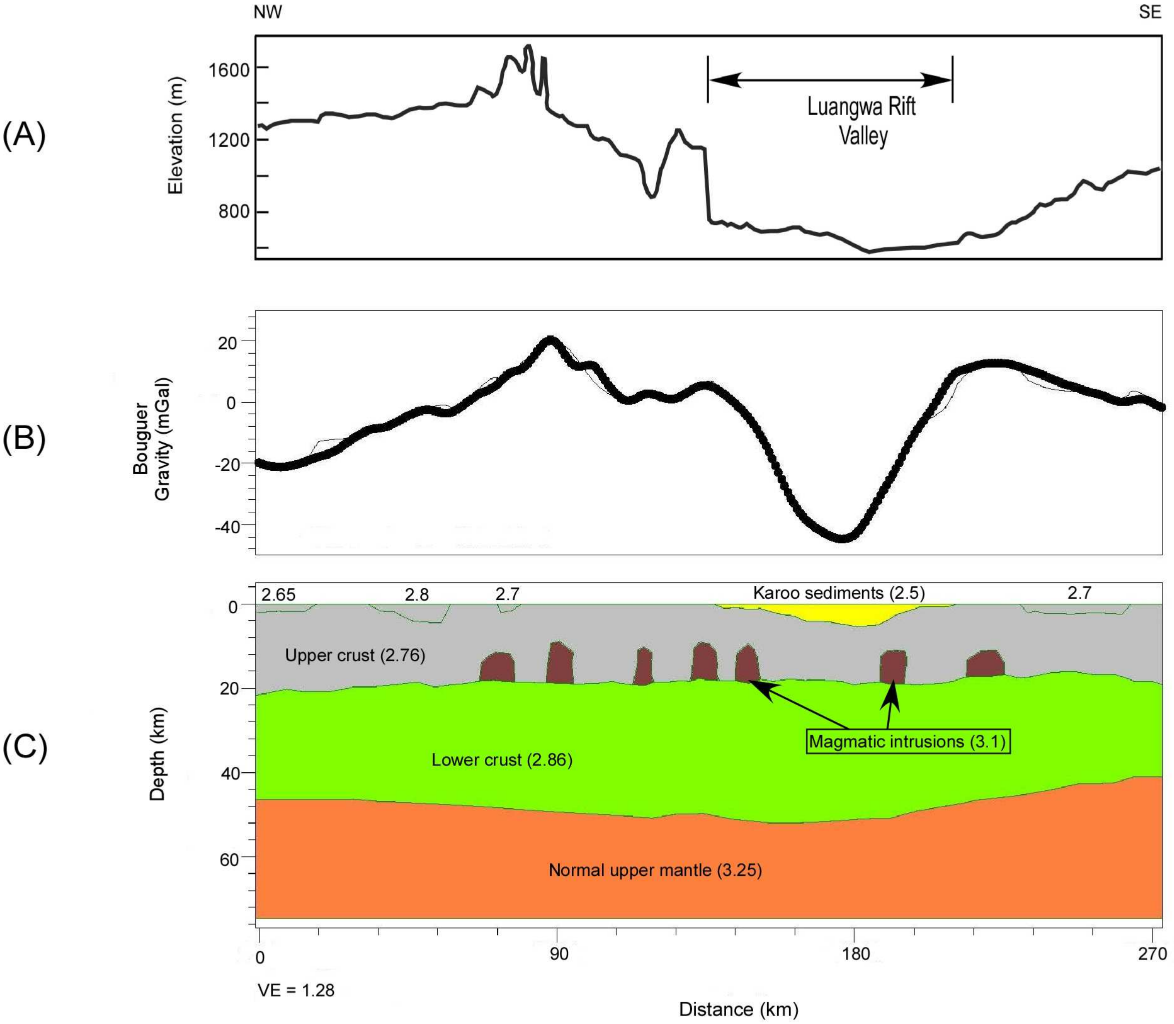

Figure 16: (A) Topography extracted from Shuttle Radar Topography Mission (SRTM) Digital Elevation Model (DEM). (B) Observed (dotted line) Bouguer gravity anomalies across the Luangwa Rift Valley (LRV) along profile B-B' and calculated (solid line) Bouguer gravity anomalies of the two-dimensional (2D) forward model in Fig. 17C. (C) A 2D gravity forward model showing a thick crust beneath the LRV. Numbers are densities in g/cm^3. See Fig. 8 for location of the profile.

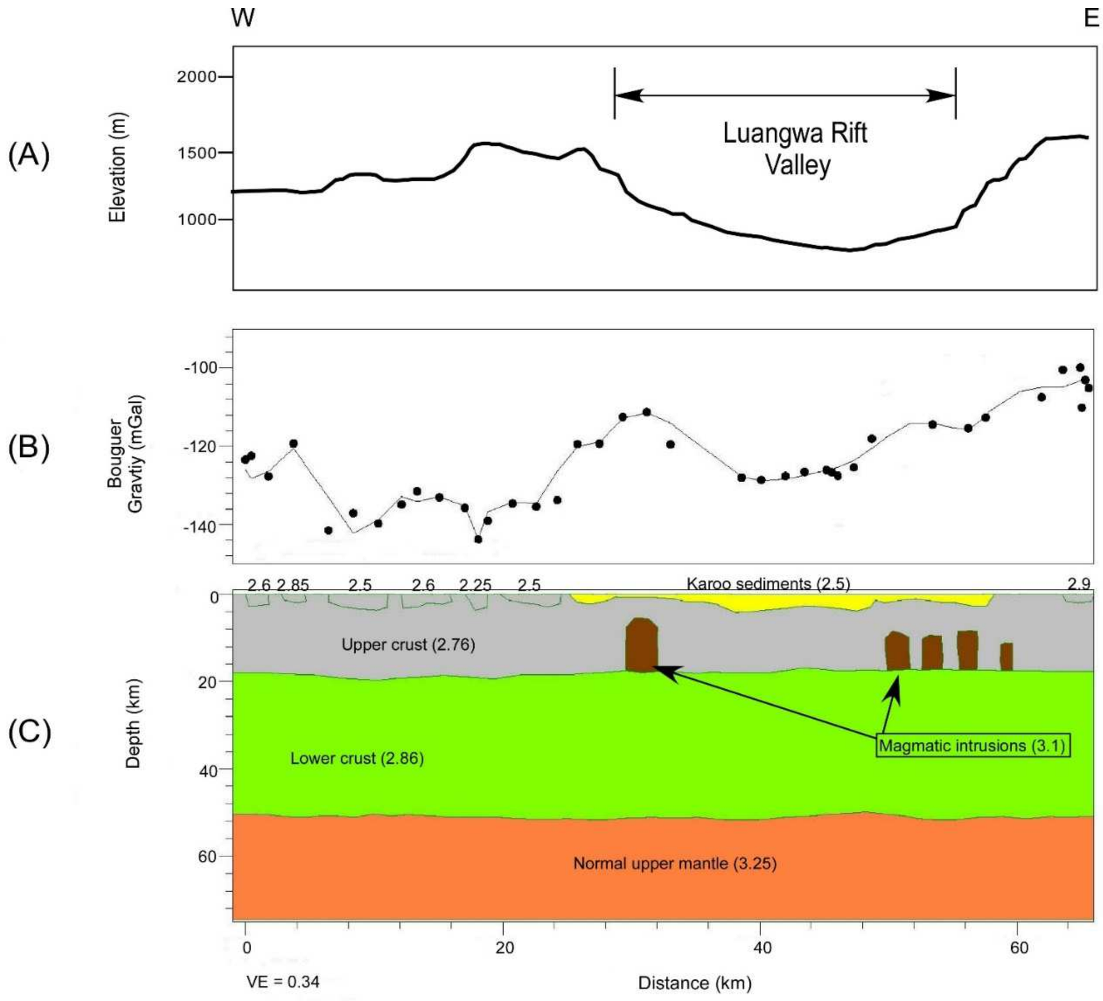

Figure 17: (A) Topography extracted from Shuttle Radar Topography Mission (SRTM) Digital Elevation Model (DEM). (B) Observed (dotted line) Bouguer gravity anomalies across the Luangwa Rift Valley (LRV) along profile C-C' and calculated (solid line) Bouguer gravity anomalies of the two-dimensional (2D) forward model in Fig. 16C. (C) A 2D gravity forward model showing a thickened crust beneath the LRV. Numbers are densities in g/cm^3. See Fig. 8 for location of the profile.

5.5 Did metacratonization/decratonization facilitate the localization of the UPMB?

Liégeois et al. (2013) suggested the granitoids observed in the Irumide and Southern Irumide belts [Fig. 2] to be representative of the metacratonization and decratonization processes, respectively, that occurred at the southern margin of the Bangweulu Block. The authors define metacratonization as the partial reworking of cratonic margins which results in orogenic belts in which old Archean lithologies are mixed with juvenile ones. Decratonization on the other hand, is defined as the complete reworking of cratonic crusts, leading to complete replacement of the old Archean lithologies by younger rocks. It is possible that the metacratonization and decratonization processes facilitated the localization of the UPMB that eventually localized extensional strain during rift formation. Fig. 18 represents a conceptual model of the evolution of the LRV. Before 1.1 Ga, the convergence between the Bangweulu Block and the Zimbabwe craton resulted in the consumption of the Irumide proto-ocean. The subductions lead to lithospheric mantle delamination due to asthenospheric flow [Fig. 18 A]. The lithospheric mantle delamination under the southern margin of the Bangweulu Block led to the formation of an asthenospheric window between 1.1 and 1.0 Ga, putting the asthenosphere directly under the base of the crust [Fig. 18 B]. This resulted in decratonization of what became the Southern Irumide belt and metacratonization of what became the Irumide belt. The metacratonization and decratonization processes weakened the subcontinental lithospheric mantle, resulting in subsequent guiding of the emplacement of the UPMB between 1.0 and 0.3 Ga [Fig. 18 C]. The weakening of the lithosphere through the combined process of decratonization, metacratonization and UPMB emplacement enhanced strain localization during the onset of rifting after 0.3 Ga, and hence the location of the LRV at the interface between the Irumide and Southern Irumide belts [Fig. 18 D].

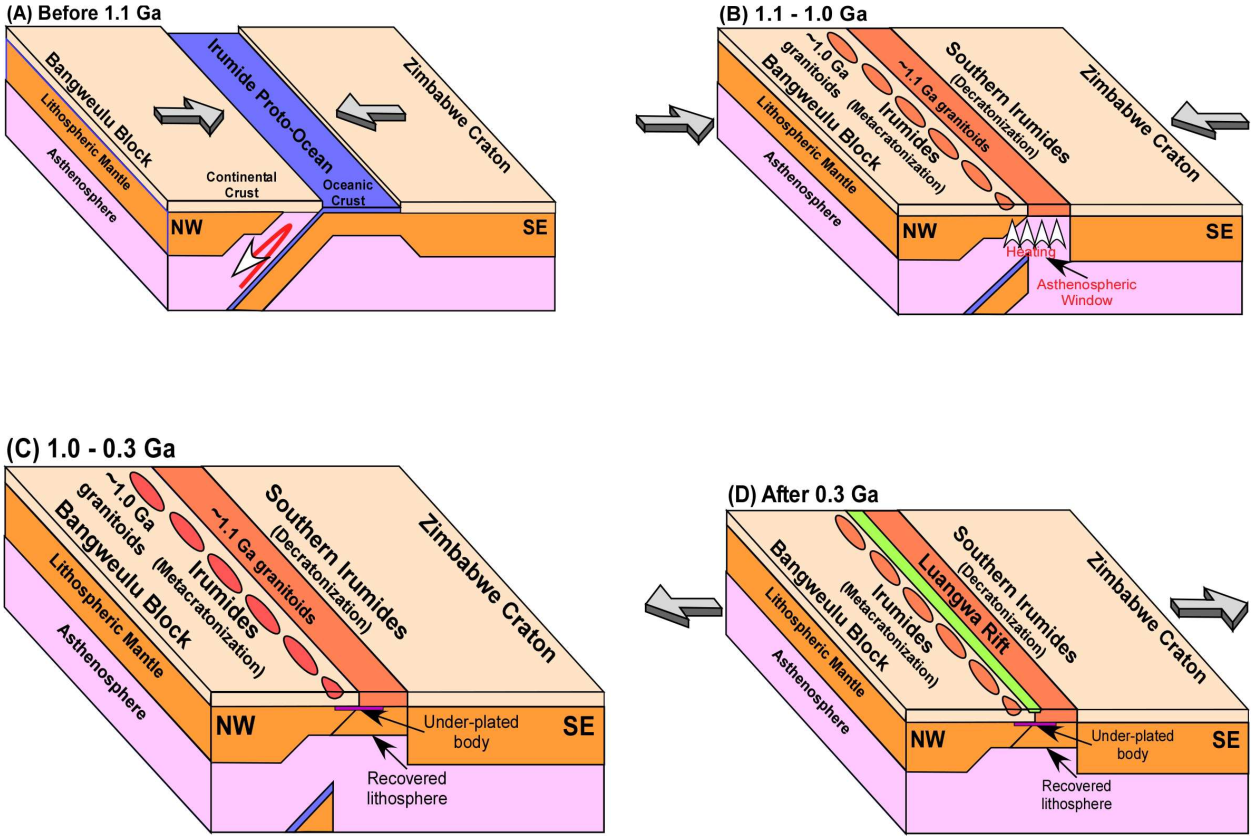

Figure 18: Conceptual model of the evolution of the LRV due to the Precambrian aged metacratonization/decratonization combined with magmatic under-plating. (A) Lithospheric mantle delamination through asthenospheric adega flow. (B) Decratonization-metacratonization of the southern edge of the Bangweulu Block. (C) Extensional strain localization through magmatic under-plating. (D) Magmatic under-plating. See text for explanation.

CHAPTER VI

CONCLUSIONS

Radially averaged 2D power spectral analyses of aeromagnetic and satellite gravity data have demonstrated the lack of thermal anomaly beneath the LRV, but a thickened crust beneath this Karoo-aged rift. Within the rift, the CPD values range from to 22 to 27 km, while heat flow ranges from 62 to 74 mW/m^2. The crustal thickness beneath the rift ranges from 40 to 55 km. Crustal thickness estimations from a passive seismic study across the LRV, differ from the gravity estimations by up to 12 km. A 2D forward model of ground gravity data across the rift suggests the presence of an UPMB that explains the observed difference in crustal thickness as estimated by gravity and passive seismic data. It is likely that the passive seismic study imaged the top of the UPMB as the Moho while the gravity analyses imaged the base of this mafic magmatic body. The weakening of the lithosphere through the combined process of decratonization and metacratonization of the southern margin of the Bangweulu Block, together with the UPMB emplacement enhanced strain localization during the onset of rifting, and hence the location of the LRV at the interface between the Irumide and Southern Irumide belts

REFERENCES

Acocella, V., Funiciello, R., Marotta, E., Orsi, G., & De Vita, S. (2004). The role of extensional structures on experimental calderas and resurgence. *Journal of Volcanology and Geothermal Research, 129*(1), 199-217.

Akimoto, S. (1962),Magnetic properties of FeO-Fe_2O_3-TiO_2 system as a basis of rock magnetism,*J. Phys. Soc. Jpn.*, **17**(suppl. B-1), 706–710.

Andersen, L., & Unrug, R. (1984). Geodynamic evolution of the Bangweulu Block, northern Zambia. *Precambrian Research, 25*(1), 187-212.

Andrews-Speed, C. (1986). Gold-bearing fluvial and associated tidal marine sediments of Proterozoic age in the Mporokoso Basin, northern Zambia. *Sedimentary geology, 48*(3), 193-222.

Artyushkov, E. (1973). Stresses in the lithosphere caused by crustal thickness inhomogeneities. *Journal of Geophysical Research, 78*(32), 7675-7708.

Ballard, S., & Pollack, H. N. (1987). Diversion of heat by Archean cratons: a model for southern Africa. *Earth and Planetary Science Letters, 85*(1), 253-264.

Balmino, G., Vales, N., Bonvalot, S., & Briais, A. (2012). Spherical harmonic modelling to ultra-high degree of Bouguer and isostatic anomalies. *Journal of Geodesy, 86*(7), 499-520.

Banks, N., Bardwell, K., & Musiwa, S. (1995). Karoo rift basins of the Luangwa Valley, Zambia. *Geological Society, London, Special Publications, 80*(1), 285-295.

Bansal, A., Gabriel, G., Dimri, V., & Krawczyk, C. (2011). Estimation of depth to the bottom of magnetic sources by a modified centroid method for fractal distribution of sources: An application to aeromagnetic data in Germany. *Geophysics, 76*(3), L11-L22.

Bassi, G. (1991). Factors controlling the style of continental rifting: insights from numerical modelling. *Earth and Planetary Science Letters, 105*(4), 430-452.

Behrendt, J., Hutchinson, D., Lee, M., Thornber, C., Trehu, A., Cannon, W., & Green, A. (1990). GLIMPCE seismic reflection evidence of deep-crustal and upper-mantle intrusions and magmatic underplating associated with the Midcontinent Rift system of North America. *Tectonophysics, 173*(1), 595-615.

Bhattacharyya, B., & Leu, L.-K. (1975). Spectral analysis of gravity and magnetic anomalies due to two-dimensional structures. *Geophysics, 40*(6), 993-1013.

Birt, C., Maguire, P., Khan, M., Thybo, H., Keller, G., & Patel, J. (1997). The influence of pre-existing structures on the evolution of the southern Kenya Rift Valley—evidence from seismic and gravity studies. *Tectonophysics, 278*(1), 211-242.

Bleil, U. (1976). An experimental study of the titanomagnetite solid solution series. *Pure and Applied Geophysics, 114*(2), 165-175.

Bonvalot, S., Balmino, G., Briais, A., Kuhn, M., Peyrefitte, A., & Vales, N. (2012). World Gravity Map, 1: 50000000 map, Eds: BGI-CGMW-CNES-IRD. Paris, 2012. http://bgi. obs-mip. fr/activities/Projects/world_gravity_map_ wgm.

Bouligand, C., Glen, J. M., & Blakely, R. J. (2009). Mapping Curie temperature depth in the western United States with a fractal model for crustal magnetization. *Journal of Geophysical Research: Solid Earth (1978–2012), 114*(B11).

Buck, W. (2006). The role of magma in the development of the Afro-Arabian Rift System. *Geological Society, London, Special Publications, 259*(1), 43-54.

Bumby, A. J., & Guiraud, R. (2005). The geodynamic setting of the Phanerozoic basins of Africa. *Journal of African Earth Sciences, 43*(1), 1-12.

Callot, J. P., Grigné, C., Geoffroy, L., & Brun, J. P. (2001). Development of volcanic passive margins: Two-dimensional laboratory models. *Tectonics, 20*(1), 148-159.

Casey, M., Ebinger, C., Keir, D., Gloaguen, R., & Mohamed, F. (2006). Strain accommodation in transitional rifts: extension by magma intrusion and faulting in Ethiopian rift magmatic segments. *SPECIAL PUBLICATION-GEOLOGICAL SOCIETY OF LONDON, 259*, 143-163.

Catuneanu, O., Wopfner, H., Eriksson, P., Cairncross, B., Rubidge, B., Smith, R., & Hancox, P. (2005). The Karoo basins of south-central Africa. *Journal of African Earth Sciences, 43*(1), 211-253.

Chapman, D. S., & Pollack, H. N. (1975). Global heat flow: a new look. *Earth and Planetary Science Letters, 28*(1), 23-32.

Chiozzi, P., Matsushima, J., Okubo, Y., Pasquale, V., & Verdoya, M. (2005). Curie-point depth from spectral analysis of magnetic data in central–southern Europe. *Physics of the Earth and Planetary Interiors, 152*(4), 267-276.

Chorowicz, J. (2005). The East African rift system. *Journal of African Earth Sciences, 43*(1), 379-410.

Coldwell, B., Clemens, J., & Petford, N. (2011). Deep crustal melting in the Peruvian Andes: felsic magma generation during delamination and uplift. *Lithos, 125*(1), 272-286.

Connard, G., Couch, R., & Gemperle, M. (1983). Analysis of aeromagnetic measurements from the Cascade Range in central Oregon. *Geophysics, 48*(3), 376-390.

Corti, G., Bonini, M., Mazzarini, F., Boccaletti, M., Innocenti, F., Manetti, P., Mulugeta, G., & Sokoutis, D. (2002). Magma-induced strain localization in centrifuge models of transfer zones. *Tectonophysics, 348*(4), 205-218.

Cox, K. G. “The Karoo Province.” *Continental flood basalts*. Springer Netherlands, 1988. 239-271.

Daly, M. (1986). The intracratonic Irumide belt of Zambia and its bearing on collision orogeny during the Proterozoic of Africa. *Geological Society, London, Special Publications, 19*(1), 321-328.

Daly, M., Chorowicz, J., & Fairhead, J. (1989). Rift basin evolution in Africa: the influence of reactivated steep basement shear zones. *Geological Society, London, Special Publications, 44*(1), 309-334.

De Waele, B., & Fitzsimons, I. (2007). The nature and timing of Palaeoproterozoic sedimentation at the southeastern margin of the Congo Craton; zircon U–Pb geochronology of plutonic, volcanic and clastic units in northern Zambia. *Precambrian Research, 159*(1), 95-116.

De Waele, B., Fitzsimons, I., Wingate, M., Tembo, F., Mapani, B., & Belousova, E. (2009). The geochronological framework of the Irumide Belt: a prolonged crustal history along the margin of the Bangweulu Craton. *American Journal of Science, 309*(2), 132-187.

De Waele, B., Kampunzu, A., Mapani, B., & Tembo, F. (2006). The Mesoproterozoic Irumide belt of Zambia. *Journal of African Earth Sciences, 46*(1), 36-70.

De Waele, B., & Mapani, B. (2002). Geology and correlation of the central Irumide belt. *Journal of African Earth Sciences, 35*(3), 385-397.

Delvaux, D. (1989). The Karoo to Recent rifting in the western branch of the East-African Rift System: A bibliographical synthesis. *Mus. roy. Afr. centr., Tervuren (Belg.), Dépt. Géol. Min., Rapp. ann, 1990*(1991), 63-83.

Delvaux, D., Levi, K., Kajara, R., & Sarota, J. (1992). Cenozoic paleostress and kinematic evolution of the Rukwa-North Malawi rift valley (East African rift system). *Bulletin des Centres de Recherche Exploration-Production Elf-Aquitaine, 16*(2), 383-406.

Dèzes, P., Schmid, S., & Ziegler, P. (2004). Evolution of the European Cenozoic Rift System: interaction of the Alpine and Pyrenean orogens with their foreland lithosphere. *Tectonophysics, 389*(1), 1-33.

Douce, A. E. P. (1999). What do experiments tell us about the relative contributions of crust and mantle to the origin of granitic magmas? *Geological Society, London, Special Publications, 168*(1), 55-75.

Drysdall, A., Johnson, R., Moore, T., & Thieme, J. (1972). Outline of the geology of Zambia. *Geol. Mijnbouw, 51*, 265-276.

Duncan, R. A., Hooper, P., Rehacek, J., Marsh, J., & Duncan, A. (1997). The timing and duration of the Karoo igneous event, southern Gondwana. *Journal of Geophysical Research: Solid Earth (1978–2012), 102*(B8), 18127-18138.

Ebinger, C., Ayele, A., Keir, D., Rowland, J., Yirgu, G., Wright, T., Belachew, M., & Hamling, I. (2010). Length and timescales of rift faulting and magma intrusion: the Afar rifting cycle from 2005 to present. *Annual Review of Earth and Planetary Sciences, 38*, 439-466.

Ebinger, C., & Casey, M. (2001). Continental breakup in magmatic provinces: An Ethiopian example. *Geology, 29*(6), 527-530.

Ebinger, C., Keir, D., Ayele, A., Calais, E., Wright, T., Belachew, M., Hammond, J. O. S., Campbell, E., & Buck, W. (2008). Capturing magma intrusion and faulting processes during continental rupture: seismicity of the Dabbahu (Afar) rift. *Geophysical Journal International, 174*(3), 1138-1152.

Ebinger, C. J., & Sleep, N. (1998). Cenozoic magmatism throughout east Africa resulting from impact of a single plume. *Nature, 395*(6704), 788-791.

England, P., & McKenzie, D. (1982). A thin viscous sheet model for continental deformation. *Geophysical Journal International, 70*(2), 295-321.

Erlank, A. (1984). *Petrogenesis of the Volcanic Rocks of the Karoo Province: National Geodynamics Programme Sponsored by the South African Council for Scientific and Industrial Research*.

Fairhead, J., & Okereke, C. (1987). A regional gravity study of the West African rift system in Nigeria and Cameroon and its tectonic interpretation. *Tectonophysics, 143*(1), 141-159.

Fairhead, J., & Stuart, G. (1982). The seismicity of the East African rift system and comparison with other continental rifts. *Continental and Oceanic Rifts*, 41-61.

Furlong, K. P., & Fountain, D. M. (1986). Continental crustal underplating: Thermal considerations and seismic-petrologic consequences. *Journal of Geophysical Research: Solid Earth (1978–2012), 91*(B8), 8285-8294.

Fyfe, W. (1978). The evolution of the Earth's crust: modern plate tectonics to ancient hot spot tectonics? *Chemical Geology, 23*(1), 89-114.

Fyfe, W. (1992). Magma underplating of continental crust. *Journal of Volcanology and Geothermal Research, 50*(1), 33-40.

Fritz, H., Abdelsalam, M., Ali, K., Bingen, B., Collins, A., Fowler, A., Ghebread, W., Hauzenberger, C., Johnson, P., Kusky, T., Macey, P., Muhongo, S., Stern, R., & Viola, G. (2013). Orogen styles in the East African Orogen: a review of the Neoproterozoic to Cambrian tectonic evolution. *Journal of African Earth Sciences, 86*, 65-106.

Fraser, S. I., Fraser, A. J., Lentini, M. R., & Gawthorpe, R. L. (2007). Return to rifts–the next wave: fresh insights into the petroleum geology of global rift basins. *Petroleum Geoscience, 13*(2), 99-104.

Gilder, S. A., & Le Goff, M. (2008). Systematic pressure enhancement of titanomagnetite magnetization. *Geophysical Research Letters, 35*(10).

Gladczenko, T. P., Coffin, M. F., & Eldholm, O. (1997). Crustal structure of the Ontong Java Plateau: modeling of new gravity and existing seismic data. *Journal of Geophysical Research: Solid Earth (1978–2012), 102*(B10), 22711-22729.

Gómez-Ortiz, D., Tejero-López, R., Babín-Vich, R., & Rivas-Ponce, A. (2005). Crustal density structure in the Spanish Central System derived from gravity data analysis (Central Spain). *Tectonophysics, 403*(1), 131-149.

Govers, R., & Wortel, M. (1993). Initiation of asymmetric extension in continental lithosphere. *Tectonophysics, 223*(1), 75-96.

Halls, H. (1982). 12: Crustal thickness in the Lake Superior region. *Geological Society of America Memoirs, 156*, 239-244.

Hay, D. E., Wendlandt, R. F., & Keller, G. R. (1995). Origin of Kenya Rift Plateau-type flood phonolites: Integrated petrologic and geophysical constraints on the evolution of the crust and upper mantle beneath the Kenya Rift. *Journal of Geophysical Research: Solid Earth (1978–2012), 100*(B6), 10549-10557.

Hinze, W. J., Allen, D. J., Fox, A. J., Sunwood, D., Woelk, T., & Green, A. G. (1992). Geophysical investigations and crustal structure of the North American Midcontinent Rift system. *Tectonophysics, 213*(1), 17-32.

Hunt, C. P., Moskowitz, B. M., & Banerjee, S. K. (1995). Magnetic properties of rocks and minerals. *Rock physics & phase relations: a handbook of physical constants*, 189-204.

Huppert, H. E., & Sparks, R. S. J. (1988). The generation of granitic magmas by intrusion of basalt into continental crust. *Journal of Petrology, 29*(3), 599-624.

Hussein, M., Mickus, K., & Serpa, L. F. (2013). Curie Point Depth Estimates from Aeromagnetic Data from Death Valley and Surrounding Regions, California. *Pure and Applied Geophysics, 170*(4), 617-632.

Illies, J. (1972). The Rhine graben rift system-plate tectonics and transform faulting. *Geophysical Surveys, 1*(1), 27-60.

Illies, J. (1975). Recent and paleo-intraplate tectonics in stable Europe and the Rhinegraben rift system. *Tectonophysics, 29*(1), 251-264.

Illies, J. H., & Greiner, G. (1978). Rhinegraben and the Alpine system. *Geological Society of America Bulletin, 89*(5), 770-782.

Jakovlev, A., Rümpker, G., Lindenfeld, M., Koulakov, I., Schumann, A., & Ochmann, N. (2011). Crustal seismic velocities of the Rwenzori region, east African rift, from local travel-time tomography: evidence for low-velocity anomalies beneath the mountain range. *Bulletin of the Seismological Society of America, 101*(2), 848-858.

Katumwehe, A., Abdelsalam, M., & Atekwana, E. (2015). The Role of Pre-existing Precambrian Structures in Rift Evolution: The Albertine and Rhino Grabens, Uganda. *Tectonophysics*

Keir, D., Ebinger, C., Stuart, G., Daly, E., & Ayele, A. (2006). Strain accommodation by magmatism and faulting as rifting proceeds to breakup: seismicity of the northern Ethiopian rift. *Journal of Geophysical Research: Solid Earth (1978–2012), 111*(B5).

Keranen, K., Klemperer, S., Gloaguen, R., & Group, E. W. (2004). Three-dimensional seismic imaging of a protoridge axis in the Main Ethiopian rift. *Geology, 32*(11), 949-952.

Koptev, A., Calais, E., Burov, E., Leroy, S., & Gerya, T. (2015). Dual continental rift systems generated by plume-lithosphere interaction. *Nature Geoscience*.

Korme, T., Acocella, V., & Abebe, B. (2004). The role of pre-existing structures in the origin, propagation and architecture of faults in the Main Ethiopian Rift. *Gondwana Research, 7*(2), 467-479.

Lachenbruch, A. H., & Sass, J. (1978). Models of an extending lithosphere and heat flow in the Basin and Range province. *Geological Society of America Memoir, 152*, 209-250.

Legg, C. (1974). *A reconnaissance survey of the hot and mineralised springs of Zambia*: Republic of Zambia, Ministry of Mines and Industry, Geological Survey.

Leseane, K., Atekwana, E. A., Mickus, K. L., Abdelsalam, M. G., Shemang, E. M., & Atekwana, E. A. (2015). Thermal perturbations beneath the incipient Okavango Rift Zone, northwest Botswana. *Journal of Geophysical Research: Solid Earth*.

Li, Y., & Oldenburg, D. W. (1996). 3-D inversion of magnetic data. *Geophysics, 61*(2), 394-408.

Liégeois, J.-P., Abdelsalam, M. G., Ennih, N., & Ouabadi, A. (2013). Metacraton: nature, genesis and behavior. *Gondwana Research, 23*(1), 220-237.

Lillie, R. J. *Whole earth geophysics- An Introductory Textbook for Geologists and Geophysicists* (Prentice Hall, Upper Saddle River, New Jersey, 1999).

Logatchev, N., & Zorin, Y. A. (1992). Baikal rift zone: structure and geodynamics. *Tectonophysics, 208*(1), 273-286.

Lynch, H. D., & Morgan, P. (1987). The tensile strength of the lithosphere and the localization of extension. *Geological Society, London, Special Publications, 28*(1), 53-65.

Mackenzie, G., Thybo, H., & Maguire, P. (2005). Crustal velocity structure across the Main Ethiopian Rift: results from two-dimensional wide-angle seismic modelling. *Geophysical Journal International, 162*(3), 994-1006.

Mahatsente, R., Jentzsch, G., & Jahr, T. (1999). Crustal structure of the Main Ethiopian Rift from gravity data: 3-dimensional modeling. *Tectonophysics, 313*(4), 363-382.

Manea, M., & Manea, V. C. (2011). Curie point depth estimates and correlation with subduction in Mexico. *Pure and Applied Geophysics, 168*(8-9), 1489-1499.

Maus, S., & Dimri, V. (1995). Potential field power spectrum inversion for scaling geology. *Journal of Geophysical Research: Solid Earth (1978–2012), 100*(B7), 12605-12616.

McConnell, R. (1972). Geological development of the rift system of eastern Africa. *Geological Society of America Bulletin, 83*(9), 2549-2572.

Mechie, J., Keller, G., Prodehl, C., Khan, M., & Gaciri, S. (1997). A model for the structure, composition and evolution of the Kenya rift. *Tectonophysics, 278*(1), 95-119.

Mengel, K., & Kern, H. (1992). Evolution of the petrological and seismic Moho-implications for the continental crust-mantle boundary. *Terra Nova, 4*(1), 109-116.

Mickus, K., Tadesse, K., Keller, G., & Oluma, B. (2007). Gravity analysis of the main Ethiopian rift. *Journal of African Earth Sciences, 48*(2), 59-69.

Mjelde, R., Goncharov, A., & Müller, R. D. (2013). The Moho: boundary above upper mantle peridotites or lower crustal eclogites? A global review and new interpretations for passive margins. *Tectonophysics, 609*, 636-650.

Mjelde, R., Kodaira, S., Shimamura, H., Kanazawa, T., Shiobara, H., Berg, E., & Riise, O. (1997). Crustal structure of the central part of the Vøring Basin, mid-Norway margin, from ocean bottom seismographs. *Tectonophysics, 277*(4), 235-257.

Morley, C., Haranya, C., Phoosongsee, W., Pongwapee, S., Kornsawan, A., & Wonganan, N. (2004). Activation of rift oblique and rift parallel pre-existing fabrics during extension and their effect on deformation style: examples from the rifts of Thailand. *Journal of Structural Geology, 26*(10), 1803-1829.

Mulibo, G. D., & Nyblade, A. A. (2013). Mantle transition zone thinning beneath eastern Africa: Evidence for a whole-mantle superplume structure. *Geophysical Research Letters, 40*(14), 3562-3566.

Nyblade, A. A., Pollack, H. N., Jones, D., Podmore, F., & Mushayandebvu, M. (1990). Terrestrial heat flow in east and southern Africa. *Journal of Geophysical Research: Solid Earth (1978–2012), 95*(B11), 17371-17384.

O'Donnell, J., Adams, A., Nyblade, A., Mulibo, G., & Tugume, F. (2013). The uppermost mantle shear wave velocity structure of eastern Africa from Rayleigh wave tomography: constraints on rift evolution. *Geophysical Journal International, 194*(2), 961-978.

Okubo, Y., Graf, R., Hansen, R., Ogawa, K., & Tsu, H. (1985). Curie point depths of the island of Kyushu and surrounding areas, Japan. *Geophysics, 50*(3), 481-494.

Orpen, J., Swain, C., Nugent, C., & Zhou, P. (1989). Wrench-fault and half-graben tectonics in the development of the Palaeozoic Zambezi Karoo Basins in Zimbabwe—the "Lower Zambezi" and "Mid-Zambezi" basins respectively—and regional implications. *Journal of African Earth Sciences, 8*(2), 215-229.

Pálfy, J., & Smith, P. L. (2000). Synchrony between Early Jurassic extinction, oceanic anoxic event, and the Karoo-Ferrar flood basalt volcanism. *Geology, 28*(8), 747-750.

Person, M., & Garven, G. (1992). Hydrologic constraints on petroleum generation within continental rift basins: theory and application to the Rhine graben (1). *American Association of Petroleum Geologists Bulletin, 76*(4), 468-488.

Pilkington, M., & Todoeschuck, J. (1990). Stochastic inversion for scaling geology. *Geophysical Journal International, 102*(1), 205-217.

Rainaud, C., Master, S., Armstrong, R., & Robb, L. (2005). Geochronology and nature of the Palaeoproterozoic basement in the Central African Copperbelt (Zambia and the Democratic Republic of Congo), with regional implications. *Journal of African Earth Sciences, 42*(1), 1-31.

Ramsay, C., & Ridgway, J. (1977). Metamorphic patterns in Zambia and their bearing on problems of Zambian tectonic history. *Precambrian Research, 4*(4), 321-337.

Raum, T., Mjelde, R., Digranes, P., Shimamura, H., Shiobara, H., Kodaira, S., Haatvedt, G., Sorenes, N., & Thorbjørnsen, T. (2002). Crustal structure of the southern part of the Vøring Basin, mid-Norway margin, from wide-angle seismic and gravity data. *Tectonophysics, 355*(1), 99-126.

Ravat, D., Pignatelli, A., Nicolosi, I., & Chiappini, M. (2007). A study of spectral methods of estimating the depth to the bottom of magnetic sources from near-surface magnetic anomaly data. *Geophysical Journal International, 169*(2), 421-434.

Riley, T. R., Leat, P. T., Curtis, M. L., Millar, I. L., Duncan, R. A., & Fazel, A. (2005). Early–Middle Jurassic dolerite dykes from Western Dronning Maud Land (Antarctica): identifying mantle sources in the Karoo large igneous province. *Journal of Petrology, 46*(7), 1489-1524.

Ring, U. (1994). The influence of preexisting structure on the evolution of the Cenozoic Malawi rift (East African rift system). *Tectonics, 13*(2), 313-326.

Ritsema, J., Nyblade, A. A., Owens, T. J., Langston, C. A., & VanDecar, J. C. (1998). Upper mantle seismic velocity structure beneath Tanzania, east Africa: Implications for the stability of cratonic lithosphere. *Journal of Geophysical Research: Solid Earth (1978–2012), 103*(B9), 21201-21213.

Rogers, J. J., Unrug, R., & Sultan, M. (1995). Tectonic assembly of Gondwana. *Journal of Geodynamics, 19*(1), 1-34.

Rosendahl, B. R. (1987). Architecture of continental rifts with special reference to East Africa. *Annual Review of Earth and Planetary Sciences, 15*, 445-503.

Ross, H. E., Blakely, R. J., & Zoback, M. D. (2006). Testing the use of aeromagnetic data for the determination of Curie depth in California. *Geophysics, 71*(5), L51-L59.

Rotstein, Y., Edel, J.-B., Gabriel, G., Boulanger, D., Schaming, M., & Munschy, M. (2006). Insight into the structure of the Upper Rhine Graben and its basement from a new compilation of Bouguer gravity. *Tectonophysics, 425*(1), 55-70.

Rousset, D., Bayer, R., Guillon, D., & Edel, J. B. (1993). Structure of the southern Rhine Graben from gravity and reflection seismic data (ECORS-DEKORP program). *Tectonophysics, 221*(2), 135-153.

Sakungo, F. K. (1988). Geothermal resources of Zambia. *Geothermics, 17*(2), 503-514.

Salem, A., Green, C., Ravat, D., Singh, K. H., East, P., Fairhead, J. D., Mogren, S., & Biegert, E. (2014). Depth to Curie temperature across the central Red Sea from magnetic data using the de-fractal method. *Tectonophysics, 624*, 75-86.

Sanchez-Rojas, J., & Palma, M. (2014). Crustal density structure in northwestern South America derived from analysis and 3-D modeling of gravity and seismicity data. *Tectonophysics, 634*, 97-115.

Schumacher, M. E. (2002). Upper Rhine Graben: role of preexisting structures during rift evolution. *Tectonics, 21*(1), 6-1-6-17.

Shay, J., & Tréhu, A. (1993). Crustal structure of the central graben of the Midcontinent Rift beneath Lake Superior. *Tectonophysics, 225*(4), 301-335.

Shuey, R., Schellinger, D., Tripp, A., & Alley, L. (1977). Curie depth determination from aeromagnetic spectra. *Geophysical Journal International, 50*(1), 75-101.

Spector, A., & Grant, F. (1970). Statistical models for interpreting aeromagnetic data. *Geophysics, 35*(2), 293-302.

Syono, Y. (1965). Magnetocrystalline anisotropy and magnetostriction of Fe_30_4-Fe_2Ti0_4 series with special application to rock magnetism, *Jpn. J. Geophys.*, **4**, 71–143.

Tanaka, A., & Ishikawa, Y. (2005). Crustal thermal regime inferred from magnetic anomaly data and its relationship to seismogenic layer thickness: The Japanese islands case study. *Physics of the Earth and Planetary Interiors, 152*(4), 257-266.

Tanaka, A., Okubo, Y., & Matsubayashi, O. (1999). Curie point depth based on spectrum analysis of the magnetic anomaly data in East and Southeast Asia. *Tectonophysics, 306*(3), 461-470.

Thybo, H., & Artemieva, I. M. (2013). Moho and magmatic underplating in continental lithosphere. *Tectonophysics, 609*, 605-619.

Thybo, H., Maguire, P., Birt, C., & Perchuć, E. (2000). Seismic reflectivity and magmatic underplating beneath the Kenya Rift. *Geophysical Research Letters, 27*(17), 2745-2748.

Thybo, H., & Nielsen, C. A. (2009). Magma-compensated crustal thinning in continental rift zones. *Nature, 457*(7231), 873-876.

Tiberi, C., Ebinger, C., Ballu, V., Stuart, G., & Oluma, B. (2005). Inverse models of gravity data from the Red Sea-Aden-East African rifts triple junction zone. *Geophysical Journal International, 163*(2), 775-787.

Tommasi, A., & Vauchez, A. (2001). Continental rifting parallel to ancient collisional belts: an effect of the mechanical anisotropy of the lithospheric mantle. *Earth and Planetary Science Letters, 185*(1), 199-210.

Trehu, A., Morel-à-l'Huissier, P., Meyer, R., Hajnal, Z., Karl, J., Mereu, R., Sexton, J., Shay, J., Chan, W.-K., Epili, D., Jefferson, T., Shih, X. –R., Wendling, S., Milkereit, B., Green, A., & Hutchinson, D. (1991). Imaging the Midcontinent Rift beneath Lake Superior using large aperture seismic data. *Geophysical Research Letters, 18*(4), 625-628.

Tselentis, G.-A., Drakopoulos, J., & Dimitriadis, K. (1988). A spectral approach to Moho depths estimation from gravity measurements in Epirus (NW Greece). *Journal of Physics of the Earth, 36*(6), 255-266.

Utting, J. (1976). Pollen and spore assemblages in the Luwumbu Coal Formation (Lower Karroo) of the North Luangwa Valley, Zambia, and their biostratigraphic significance. *Review of Palaeobotany and Palynology, 21*(4), 295-315.

van Wijk, J., Baldridge, W., van Hunen, J., Goes, S., Aster, R., Coblentz, D., Grand, S., & Ni, J. (2010). Small-scale convection at the edge of the Colorado Plateau: Implications for topography, magmatism, and evolution of Proterozoic lithosphere. *Geology, 38*(7), 611-614.

Vink, G. E., Morgan, W. J., & Zhao, W. L. (1984). Preferential rifting of continents: a source of displaced terranes. *Journal of Geophysical Research: Solid Earth (1978–2012), 89*(B12), 10072-10076.

Whaler, K., & Hautot, S. (2006). The electrical resistivity structure of the crust beneath the northern Main Ethiopian Rift. *SPECIAL PUBLICATION-GEOLOGICAL SOCIETY OF LONDON, 259*, 293-305.

Wölbern, I., Rümpker, G., Schumann, A., & Muwanga, A. (2010). Crustal thinning beneath the Rwenzori region, Albertine rift, Uganda, from receiver-function analysis. *International Journal of Earth Sciences, 99*(7), 1545-1557.

Yamasaki, T., & Gernigon, L. (2009). Styles of lithospheric extension controlled by underplated mafic bodies. *Tectonophysics, 468*(1), 169-184.

Yu, Y., Reed, C., Gao, S., Liu, K., Massinque, B., Mdala, H., Moidaki, M., Mutamina, D. M., Atekwana, E. A., Ingate, S. F., Reusch, A. M., & Barstow, N. (2013). *Crustal and mantle structure and anisotropy beneath the incipient segments of the East African Rift System: Preliminary results from the ongoing SAFARI.* Paper presented at the AGU Fall Meeting Abstracts.

APPENDIX I

Data Management Plan

I. Types of Data

Ground gravity data were collected across the Luangwa Rift Valley in Zambia along major roads at 2 km station spacing. The data was collected using a Scintrex CG5 Autograv with differential GPS receivers (TOPCON). The gravity data were also tied to a 1971 IGSN (International Gravity Standardization NET) absolute gravity stations. Additional data used included satellite gravity data from the World Gravity Map 2012 (WGM12) downloaded from the Bureau Gravimetrique International website. The aeromagnetic data were purchased from the Geological Survey Department of Zambia in Lusaka, Zambia.

II. Data and Metadata Standards

The processed ground gravity data includes the latitude, longitude, elevation, observed gravity value tied to the IGSN station, and the Bouguer gravity anomaly (using 2.67 g/cc as a reduction density). The WGM12 model comprises of surface gravity measurements (from land, airborne and marine surveys), and satellite gravimetry (from the GRACE mission). The Bouguer gravity data were computed using the spherical correction instead of the regular slab correction. The international geomagnetic reference field (IGRF) has been removed from the aeromagnetic data.

III. Policies for Access and Sharing

The ground gravity data, description of the data analysis, and data interpretation will be publicized through presentations at national and international meeting, as well as publication in peer review journals. The data will also be made available through the GeoPRISMS website (http://geoprisms.org/). The satellite gravity data can be downloaded from http://bgi.omp.obs-mip.fr/data-products/Toolbox/WGM2012-maps-vizualisation-extraction. The aeromagnetic data can be acquired through the Geological Survey Department of Zambia.

Any researcher seeking to perform repeatability of this project's tasks or manipulate the data for other processing schemes not included in this project proposal may do so by accessing the data collected during this research study.

IV. Policies and Provisions for Re-Use, Re-Distribution

The PIs will not put any restrictions on the use of the gravity data once publicly available. There are no economic, political or other embargoes that will be placed on the use of the data, nor privacy or ethical issues that will constrain the release of this data to the general public. Once published and made available in a publicly accessible data storage, the data can be used for any purpose deem fit by any user.

V. Plans for Archiving and Preservation of Access

The ground gravity data will be given to GeoPRISMS for access by the public. Furthermore, geophysical data will be available in publications that result from these studies.

APPENDIX II

Latitude (deg.)	Longitude (deg.)	Elevation (m)	Observed gravity (mGal)	Bouguer gravity (mGal)
-13.56334	32.589241	1011.631	978015	-101.37
-13.55024	32.587559	1009.711	978018.19	-98.03
-13.53921	32.574039	980.9074	978018.69	-102.77
-13.53138	32.558403	978.2861	978017.31	-104.41
-13.53114	32.541328	992.886	978021.94	-96.9
-13.52771	32.521626	957.2549	978024.5	-101.17
-13.51876	32.508888	954.024	978024.88	-101.13
-13.51048	32.479069	922.9649	978022.63	-109.08
-13.50845	32.459301	924.9156	978017.44	-113.89
-13.50369	32.443821	940.5214	978020.75	-107.27
-13.49292	32.427608	910.9253	978015.31	-118.11
-13.49109	32.413204	938.7535	978014.06	-113.79
-13.48794	32.394669	927.2016	978013.81	-116.22
-13.48712	32.378674	923.9707	978014.19	-116.44
-13.47906	32.362003	924.367	978013.63	-116.59
-13.46804	32.353485	921.959	978013.5	-116.69
-13.45289	32.348282	918.1795	978021.69	-107.76

Latitude (deg.)	Longitude (deg.)	Elevation (m)	Observed gravity (mGal)	Bouguer gravity (mGal)
-13.4386	32.338135	886.9985	978031.88	-103.64
-13.42756	32.325245	843.2902	978034.88	-109.11
-13.40893	32.315739	822.96	978032.44	-114.86
-13.39566	32.315807	808.4515	978031.88	-117.74
-13.37909	32.30912	805.8607	978029.81	-119.67
-13.36293	32.297886	795.7718	978034.63	-116.16
-13.35349	32.286194	770.5344	978034.19	-121.15
-13.3303	32.265495	743.4682	978041	-118.73
-13.32107	32.252884	729.4474	978039.94	-122.17
-13.31206	32.237141	718.627	978036.5	-127.38
-13.3054	32.221531	718.7794	978041.69	-121.9
-13.29186	32.21093	681.8071	978045.44	-124.79
-13.28559	32.194485	658.8252	978040.88	-133.63
-13.27324	32.183311	639.4094	978042.56	-135.23
-13.25565	32.179081	632.3381	978040.75	-137.72
-13.26132	32.160858	622.5235	978039.5	-141.11
-13.26717	32.144753	622.615	978039.44	-141.41
-13.27244	32.12785	615.0254	978039.56	-142.97
-13.27478	32.10976	608.5027	978041.69	-142.24

Latitude (deg.)	Longitude (deg.)	Elevation (m)	Observed gravity (mGal)	Bouguer gravity (mGal)
-13.28735	32.097042	603.1992	978043.06	-142.4
-13.29445	32.08181	600.1207	978051.38	-134.96
-13.29751	32.047424	590.3976	978053.94	-134.43
-13.3053	32.031342	604.266	978051.44	-134.49
-13.29748	32.023022	591.373	978053.75	-134.39
-13.28601	32.012028	586.0085	978054.44	-134.35
-13.28191	31.996227	577.5046	978054	-136.3
-13.26616	31.985594	570.799	978048.31	-142.68
-13.25135	31.973709	566.6842	978057.88	-133.36
-13.23717	31.962902	562.5998	978060.13	-131.33
-13.22256	31.957289	558.9118	978057.94	-133.65
-13.20888	31.943541	555.2542	978051.5	-140.23
-13.20586	31.927736	548.2438	978052.13	-140.86
-13.19889	31.910286	547.6951	978065.06	-127.77
-13.19177	31.895903	546.415	978069.75	-123.02
-13.18027	31.878746	546.1711	978067	-125.35
-13.17532	31.864861	542.9098	978068.88	-123.91
-13.15723	31.860176	539.0083	978068.06	-124.75
-13.14409	31.855255	536.9966	978066.81	-125.88

Latitude (deg.)	Longitude (deg.)	Elevation (m)	Observed gravity (mGal)	Bouguer gravity (mGal)
-13.13682	31.837379	533.9791	978063.44	-129.54
-13.12588	31.828262	531.0835	978061.38	-131.76
-13.11028	31.796686	526.9078	978053.56	-139.75
-13.09952	31.786102	530.6263	978049.31	-142.79
-13.11378	31.810297	527.6698	978059.19	-134.11
-13.0823	31.786236	525.6276	978048.06	-144.38
-13.06622	31.787148	528.6146	978044.38	-146.8
-13.05069	31.780434	530.3825	978041.88	-148.38
-13.05443	31.777988	528.5842	978043.19	-147.55
-13.0556	31.759485	535.0459	978046.5	-142.96
-13.06158	31.745695	531.0226	978050.69	-139.78
-13.07577	31.737753	527.7917	978054.56	-137.08
-13.08995	31.730219	531.876	978056.75	-134.61
-13.10359	31.725433	529.4681	978060.44	-131.96
-13.11228	31.700752	550.3164	978060.75	-127.96
-13.11932	31.675333	571.1952	978049.69	-135.17
-13.11827	31.647919	615.5131	978038.19	-137.92
-13.12124	31.621622	671.5049	978030.5	-134.58
-13.09907	31.610733	695.9498	978026.81	-132.58

Latitude (deg.)	Longitude (deg.)	Elevation (m)	Observed gravity (mGal)	Bouguer gravity (mGal)
-13.06687	31.578753	699.1502	978028.56	-129
-13.06974	31.555784	751.393	978018.19	-128.86
-13.04691	31.541231	712.7443	978024.38	-129.6
-13.0417	31.535526	703.9051	978025.75	-129.72
-13.01634	31.544323	667.0548	978031.69	-130.14
-13.01988	31.513445	791.6875	978029.75	-107.42
-12.99361	31.536236	831.9821	978025.31	-102.8
-12.96979	31.538239	843.4121	978019.25	-105.67
-12.95016	31.526733	863.5289	978015.13	-104.9
-12.92452	31.532852	873.8006	978013.38	-103.65
-12.88025	31.521994	862.0963	978011.63	-105.91
-12.86846	31.503246	856.3051	978009.13	-109.07
-12.85046	31.481831	859.0788	978002.38	-114.35
-12.83938	31.463417	869.3201	977995.69	-118.37
-12.82009	31.46056	891.0218	977988.19	-120.65
-12.79811	31.461887	896.6911	977984.88	-121.95
-13.57233	32.596325	1029.035	978018.38	-94.9
-13.5891	32.601238	1047.841	978018.75	-91.39
-13.60479	32.608665	1081.522	978011.19	-92.92

Latitude (deg.)	Longitude (deg.)	Elevation (m)	Observed gravity (mGal)	Bouguer gravity (mGal)
-13.61967	32.619846	1088.959	978009.81	-93.36
-13.63213	32.629669	1119.957	978004	-93.13
-13.64053	32.646164	1147.999	977998.38	-93.71
-11.20129	28.891233	1207.922	977819.56	-169.46
-11.20686	28.918852	1205.545	977821.69	-168
-11.21645	28.943485	1224.991	977818.63	-167.56
-11.22981	28.971214	1218.499	977824.56	-163.38
-11.24589	28.999987	1236.238	977820.69	-164.34
-11.25907	29.019682	1253.399	977820.56	-161.52
-11.26493	29.050217	1239.744	977831	-153.95
-11.26855	29.07597	1260.683	977831.25	-149.7
-11.27256	29.103979	1220.175	977844.31	-144.77
-11.27357	29.132879	1229.289	977843.38	-143.96
-11.27252	29.158655	1238.128	977839.56	-145.98
-11.27115	29.189968	1228.527	977840.88	-146.54
-11.27108	29.195358	1222.736	977842.88	-145.64
-11.26992	29.218739	1222.614	977845.38	-143.15
-11.26921	29.246288	1223.223	977847.5	-140.9
-11.27622	29.275003	1251.113	977841.81	-141.31

Latitude (deg.)	Longitude (deg.)	Elevation (m)	Observed gravity (mGal)	Bouguer gravity (mGal)
-11.28334	29.302143	1259.495	977841.88	-139.81
-11.29317	29.329987	1221.303	977854	-135.55
-11.30451	29.355509	1180.247	977868.44	-129.56
-11.31663	29.382368	1200.302	977867.19	-127.33
-11.33081	29.405563	1198.474	977875.88	-119.5
-11.36076	29.45363	1197.834	977875.25	-121.33
-11.35481	29.478809	1204.173	977872.38	-122.76
-11.36967	29.495754	1194.938	977871.06	-126.37
-11.39694	29.498329	1207.679	977873.56	-122.31
-11.41632	29.496456	1214.354	977870.25	-125
-11.43769	29.494459	1199.479	977871.94	-127
-11.45609	29.492346	1213.592	977867.19	-129.58
-11.46608	29.47666	1207.252	977868.38	-130.02
-11.47436	29.459209	1209.172	977868.19	-130.1
-11.48595	29.446447	1196.37	977871.56	-129.66
-11.50456	29.43854	1197.224	977873.63	-128.08
-11.52282	29.438112	1189.116	977875.69	-128.29
-11.54212	29.439865	1192.835	977872.94	-130.95
-11.56131	29.441591	1191.036	977872.5	-132.44

Latitude (deg.)	Longitude (deg.)	Elevation (m)	Observed gravity (mGal)	Bouguer gravity (mGal)
-11.57965	29.443245	1204.966	977868.13	-134.73
-11.59946	29.44504	1205.728	977866.25	-137.09
-11.61729	29.446997	1189.452	977867.81	-139.42
-11.63424	29.454952	1181.74	977868.81	-140.53
-11.65115	29.463615	1180.003	977869	-141.3
-11.66755	29.472006	1181.405	977869.25	-141.37
-11.68474	29.480804	1178.54	977872.19	-139.58
-11.70015	29.488609	1175.675	977874.81	-138.07
-11.71852	29.498112	1178.296	977874.69	-138.35
-11.73176	29.504887	1181.405	977875.31	-137.59
-11.75243	29.514486	1191.402	977872.31	-139.33
-11.76659	29.51432	1190.427	977871.88	-140.49
-11.7902	29.513607	1178.204	977875.5	-140.13
-11.80665	29.513128	1206.917	977875	-135.57
-11.82688	29.506302	1216.944	977874.44	-134.9
-11.84417	29.498123	1236.147	977870.63	-135.5
-11.8611	29.489923	1226.302	977874	-134.72
-11.87743	29.481993	1159.246	977876.13	-146.42
-11.89499	29.473503	1157.813	977877.5	-145.94

Latitude (deg.)	Longitude (deg.)	Elevation (m)	Observed gravity (mGal)	Bouguer gravity (mGal)
-11.91158	29.467218	1198.931	977876.69	-139.26
-11.93073	29.472788	1177.656	977875.31	-145.52
-11.94811	29.479155	1209.66	977872.63	-142.52
-11.95845	29.495625	1201.217	977873.31	-143.93
-11.967	29.510485	1199.723	977872.06	-145.75
-11.97729	29.528576	1205.332	977869.56	-147.53
-11.98688	29.545626	1218.194	977867.38	-147.51
-11.99611	29.562012	1208.075	977868.5	-148.78
-12.00568	29.578686	1201.613	977868.19	-150.69
-12.01517	29.595154	1226.363	977869.06	-145.27
-12.02485	29.612024	1186.495	977872.81	-149.72
-12.0339	29.628231	1172.474	977877.56	-148.11
-12.04305	29.644337	1170.371	977879.75	-146.62
-12.05209	29.660234	1166.073	977881.56	-145.99
-12.06134	29.676462	1166.256	977883.13	-144.78
-12.06965	29.692307	1168.237	977884.44	-143.39
-12.07528	29.70973	1166.835	977885.5	-142.78
-12.08075	29.727274	1168.817	977885.94	-142.16
-12.08622	29.744776	1166.409	977888.31	-140.48

Latitude (deg.)	Longitude (deg.)	Elevation (m)	Observed gravity (mGal)	Bouguer gravity (mGal)
-12.09166	29.762295	1165.433	977888.94	-140.24
-12.09715	29.779875	1165.769	977887.5	-141.79
-12.10257	29.79734	1165.708	977886.13	-143.36
-12.1074	29.814207	1166.622	977884.44	-145.08
-12.11173	29.831963	1167.811	977884.44	-145.02
-12.11631	29.850634	1167.536	977887.38	-142.26
-12.12144	29.868216	1165.921	977889.63	-140.53
-12.1317	29.883341	1165.647	977892.63	-137.96
-12.14212	29.898357	1165.403	977894.88	-136.16
-12.15257	29.913355	1165.708	977896.06	-135.27
-12.163	29.928364	1166.531	977896.75	-134.83
-12.17729	29.940092	1165.281	977898.88	-133.48
-12.19207	29.949999	1166.652	977899.94	-132.71
-12.2071	29.960197	1169.548	977900.44	-132.17
-12.22213	29.970383	1171.133	977900.56	-132.29
-12.23717	29.980616	1171.56	977901.69	-131.64
-12.25219	29.990841	1172.017	977903.69	-130.14
-12.26722	30.00106	1174.212	977905.94	-127.99
-12.28225	30.011284	1176.071	977909	-125.13

Latitude (deg.)	Longitude (deg.)	Elevation (m)	Observed gravity (mGal)	Bouguer gravity (mGal)
-12.29497	30.023989	1176.345	977911.31	-123.23
-12.30502	30.039246	1176.406	977913.56	-121.33
-12.31508	30.05452	1177.016	977917	-118.2
-12.32515	30.069786	1180.49	977918.5	-116.39
-12.33523	30.085039	1183.538	977917.81	-116.81
-12.34529	30.100309	1188.415	977918.56	-115.53
-12.35536	30.115572	1188.415	977920.31	-114.11
-12.36462	30.131264	1188.049	977922.81	-112.05
-12.37187	30.148102	1192.073	977924.31	-109.99
-12.37912	30.164963	1189.97	977929.63	-105.38
-12.38635	30.181784	1189.269	977933.81	-101.65
-12.39361	30.198652	1193.627	977935.06	-99.78
-12.40066	30.215153	1192.256	977937.44	-97.94
-12.4081	30.232336	1200.333	977937	-97.07
-12.41751	30.247942	1200.241	977936.44	-98.02
-12.42863	30.26243	1207.282	977932.38	-101.11
-12.43975	30.276943	1212.555	977928.88	-103.99
-12.45088	30.291437	1208.471	977925.63	-108.41
-12.46201	30.305931	1215.603	977919.75	-113.32

Latitude (deg.)	Longitude (deg.)	Elevation (m)	Observed gravity (mGal)	Bouguer gravity (mGal)
-12.47313	30.320442	1214.171	977917	-116.8
-12.48425	30.334936	1221.76	977911.88	-120.83
-12.49538	30.349442	1223.894	977908.19	-124.51
-12.5065	30.363939	1233.861	977906.38	-124.76
-12.51762	30.378445	1244.895	977901.69	-127.67
-12.53087	30.39023	1234.044	977901.69	-130.31
-12.54893	30.391108	1229.746	977902	-131.51
-12.56697	30.391825	1237.061	977901.25	-131.56
-12.58504	30.392567	1244.773	977900.81	-131.13
-12.60308	30.393299	1237.61	977903.38	-130.67
-12.62114	30.394051	1235.385	977904.5	-130.66
-12.63918	30.394791	1257.635	977899.25	-132.21
-12.65724	30.395544	1270.041	977897.38	-132.35
-12.67518	30.396387	1279.855	977894.88	-133.52
-12.74455	30.416426	1360.048	977880.38	-134.91
-12.76176	30.422068	1384.28	977876.81	-134.31
-12.77941	30.421049	1407.688	977872.94	-134.15
-12.79682	30.416096	1438.443	977867.81	-133.79
-12.81422	30.411129	1438.747	977868.06	-134.26

Latitude (deg.)	Longitude (deg.)	Elevation (m)	Observed gravity (mGal)	Bouguer gravity (mGal)
-12.83163	30.406164	1437.833	977870.31	-132.92
-12.84903	30.401253	1413.754	977876.38	-132.3
-12.86589	30.406519	1436.583	977872.63	-132.12
-12.88217	30.414492	1436.675	977874	-131.46
-12.91242	30.434034	1443.716	977872.5	-132.72
-12.92594	30.446239	1441.125	977872.19	-134.1
-12.9396	30.458233	1460.754	977867.63	-135.29
-12.95735	30.457876	1480.475	977863.94	-135.74
-12.97521	30.455151	1516.837	977857.44	-135.69
-12.99295	30.455032	1536.162	977854.25	-135.64
-13.00538	30.458691	1563.045	977847.06	-137.97
-13.0243	30.477346	1588.648	977843.69	-137
-13.04133	30.489481	1603.858	977837	-141.31
-13.05729	30.500046	1596.603	977837.5	-142.91
-13.06636	30.518089	1588.13	977837.88	-144.62
-13.06997	30.535879	1589.471	977837.94	-144.45
-13.06999	30.551556	1606.326	977841.56	-137.42
-13.07831	30.567232	1620.012	977841.31	-135.13
-13.08355	30.582478	1601.389	977848.19	-132.3

Latitude (deg.)	Longitude (deg.)	Elevation (m)	Observed gravity (mGal)	Bouguer gravity (mGal)
-13.07938	30.600771	1619.738	977845.69	-130.89
-13.07254	30.617802	1628.242	977843.63	-130.94
-13.06975	30.635647	1629.827	977839.44	-134.73
-13.05841	30.645227	1642.293	977831.31	-139.9
-13.05903	30.663452	1607.454	977836.06	-142.21
-13.06383	30.681206	1591.696	977837.63	-144
-13.07171	30.697678	1601.876	977834.63	-145.24
-13.0773	30.714701	1599.956	977835.94	-144.51
-13.07487	30.732246	1609.009	977833.44	-145.05
-13.08385	30.748045	1582.704	977841.63	-142.46
-13.09528	30.760572	1574.353	977845.75	-140.36
-13.10453	30.775908	1567.282	977847.75	-140
-13.11612	30.789961	1628.455	977838.88	-136.89
-13.12829	30.80559	1582.613	977843.44	-142.03
-13.13923	30.818016	1572.951	977844.94	-142.81
-13.15041	30.831778	1558.046	977850.31	-140.84
-13.1554	30.847971	1537.106	977854.25	-141.32
-13.16281	30.864775	1528.481	977859.13	-138.35
-13.16692	30.881882	1517.081	977862.63	-137.2

Latitude (deg.)	Longitude (deg.)	Elevation (m)	Observed gravity (mGal)	Bouguer gravity (mGal)
-13.17307	30.899805	1506.474	977865.56	-136.5
-13.17363	30.916857	1540.002	977859.38	-135.49
-13.1768	30.934834	1525.676	977864.38	-133.75
-13.18507	30.950354	1528.237	977865.69	-132.22
-13.19287	30.966482	1509.827	977871.94	-129.75
-13.19165	30.984135	1478.981	977877.13	-130.77
-13.19864	31.000669	1505.041	977871.25	-131.28
-13.20133	31.017775	1473.251	977878.94	-130.14
-13.20065	31.036018	1472.123	977882.38	-126.71
-13.19758	31.041716	1457.035	977886.13	-125.75
-13.19785	31.060507	1512.814	977878.44	-121.81
-13.20281	31.076279	1538.661	977875.56	-119.09
-13.21871	31.084482	1541.282	977876.75	-116.85
-13.23095	31.085024	1524.64	977879.38	-117.57
-13.24703	31.078186	1559.905	977873.69	-116.12
-13.26037	31.072281	1559.387	977875	-115.09
-13.27729	31.074076	1571.031	977872	-113.71
-13.29117	31.064835	1515.161	977884.81	-112.94
-13.30476	31.055502	1514.917	977884.69	-110.95

Latitude (deg.)	Longitude (deg.)	Elevation (m)	Observed gravity (mGal)	Bouguer gravity (mGal)
-13.31825	31.04468	1523.451	977879.25	-109.24
-13.31887	31.024874	1379.129	977912.5	-113.47
-13.33244	31.014225	1245.138	977937.19	-116.26
-10.21704	31.135836	1375.105	977772.75	-150.77
-10.21704	31.135836	1386.2	977772.75	-148.56
-10.21816	31.142185	1380.287	977774.5	-148.05
-10.2118	31.160452	1379.647	977775.56	-146.97
-10.20567	31.178112	1398.697	977773.69	-144.81
-10.2011	31.192997	1396.716	977772.06	-146.75
-10.20341	31.209589	1405.402	977772.81	-144.33
-10.20501	31.229862	1408.877	977771.5	-145.01
-10.21253	31.245314	1420.581	977776	-138.3
-10.21015	31.264696	1401.836	977779.56	-138.51
-10.20216	31.300566	1408.42	977780.5	-136.05
-10.20668	31.317827	1410.34	977783.25	-133.01
-10.211	31.337393	1395.71	977781.31	-138
-10.21263	31.355366	1406.561	977778.56	-138.62
-10.21328	31.375362	1418.722	977780.56	-134.2
-10.20833	31.392752	1409.974	977785.13	-131.27

Latitude (deg.)	Longitude (deg.)	Elevation (m)	Observed gravity (mGal)	Bouguer gravity (mGal)
-10.19947	31.412052	1389.553	977789.44	-130.77
-10.19224	31.427538	1366.327	977788.13	-136.47
-10.18783	31.463806	1405.981	977782.38	-134.07
-10.19009	31.48217	1408.085	977784.06	-132.08
-10.18691	31.501104	1395.588	977787.25	-131.22
-10.17948	31.517609	1378.458	977790.94	-130.72
-10.17097	31.535734	1331.214	977799.81	-130.99
-10.15751	31.547396	1328.532	977799.75	-131.2
-10.14262	31.558187	1318.839	977801.06	-131.34
-10.13094	31.571043	1309.543	977803.56	-130.28
-10.13032	31.573364	1305.763	977807	-127.57
-10.12534	31.59194	1301.892	977803.63	-131.56
-10.12039	31.6103	1319.814	977803.94	-127.57
-10.11571	31.627708	1317.01	977805.38	-126.51
-10.11099	31.64736	1310.731	977804.88	-128.08
-10.10735	31.665407	1314.054	977811.31	-120.9
-10.10468	31.678122	1285.372	977815.38	-122.39
-10.1023	31.68442	1266.505	977810.56	-130.82
-10.10037	31.702604	1281.806	977812.88	-125.51

Latitude (deg.)	Longitude (deg.)	Elevation (m)	Observed gravity (mGal)	Bouguer gravity (mGal)
-10.09778	31.738922	1277.722	977815.5	-123.51
-10.08387	31.750671	1310.975	977815.25	-116.83
-10.0733	31.765783	1315.791	977816.44	-114.37
-10.0684	31.784882	1307.927	977813.19	-119
-10.06128	31.80106	1265.011	977814.25	-126.17
-10.053	31.817001	1251.692	977811.88	-130.87
-10.04324	31.831953	1258.611	977811.31	-129.77
-10.0336	31.847496	1265.316	977813.88	-125.61
-10.02956	31.865124	1249.985	977813	-129.33
-10.0323	31.901453	1255.044	977813.31	-128.04
-10.02905	31.921112	1230.142	977818.5	-127.72
-10.01828	31.93634	1207.404	977822.56	-127.89
-10.00881	31.950439	1210.605	977822.25	-127.31
-10.00449	31.967905	1210.422	977822.44	-127.05
-10.00382	31.986202	1210.483	977823	-126.44
-10.00243	32.00581	1210.147	977822.75	-126.71
-10.00087	32.021927	1209.69	977822.13	-127.38
-9.999096	32.039803	1214.079	977821.56	-127.05
-9.997937	32.060814	1214.171	977821.06	-127.46

Latitude (deg.)	Longitude (deg.)	Elevation (m)	Observed gravity (mGal)	Bouguer gravity (mGal)
-9.997337	32.076946	1214.14	977820.31	-128.24
-10.00168	32.095448	1210.056	977820.44	-129
-10.00545	32.111115	1209.507	977820.44	-129.24
-10.00986	32.123558	1208.41	977820.69	-129.25
-10.01464	32.141502	1209.05	977835.06	-114.71
-10.01236	32.159542	1229.533	977827.5	-118.07
-10.01452	32.17482	1270.406	977820	-116.68
-10.00166	32.187187	1293.114	977810.44	-121.43
-9.988639	32.199768	1331.062	977813	-111.45
-9.98021	32.215126	1324.874	977812.69	-112.73
-9.977786	32.23275	1331.702	977820.56	-103.72
-9.989205	32.245338	1299.362	977825.63	-105.64
-9.996087	32.265038	1283.818	977828.81	-105.88
-10.00872	32.292496	1283.147	977826.81	-108.38
-10.02171	32.305023	1284.305	977826.5	-108.84
-10.0239	32.308998	1283.879	977826.06	-109.43
-10.03466	32.315067	1287.506	977824.69	-110.41
-10.05217	32.317173	1309.268	977822.75	-108.49
-10.07159	32.319565	1329.842	977817.25	-110.48

Latitude (deg.)	Longitude (deg.)	Elevation (m)	Observed gravity (mGal)	Bouguer gravity (mGal)
-10.08075	32.334007	1385.59	977801.88	-114.82
-10.08206	32.352234	1451.275	977786.19	-117.21
-10.08077	32.370186	1542.318	977767.19	-117.75
-10.08688	32.387455	1550.457	977766.25	-117.29
-10.09482	32.389736	1515.679	977763.75	-127.24
-10.10944	32.420795	1540.947	977767.06	-119.55
-10.1118	32.437817	1506.169	977758.81	-135.02
-10.11611	32.455982	1480.261	977764.38	-134.84
-10.12693	32.470997	1469.654	977767.25	-134.43
-10.14181	32.48407	1459.139	977766.94	-137.32
-10.14664	32.500813	1439.113	977768.81	-139.54
-10.16251	32.533653	1452.189	977773.25	-132.9
-10.17256	32.549931	1481.816	977765.81	-134.56
-10.17982	32.586231	1504.462	977768.69	-127.04
-10.18084	32.604439	1505.468	977760.13	-135.19
-10.18225	32.64822	1375.837	977790.56	-130.8
-10.16948	32.661587	1363.828	977792.94	-130.32
-10.1479	32.6702	1325.331	977801.19	-129.09
-10.14555	32.687878	1187.166	977841.25	-115.32

Latitude (deg.)	Longitude (deg.)	Elevation (m)	Observed gravity (mGal)	Bouguer gravity (mGal)
-10.15974	32.697689	1152.418	977835.38	-128.88
-10.17602	32.699883	1122.914	977847.75	-122.35
-10.1972	32.700203	1086.612	977847.69	-129.78
-10.21029	32.70409	1086.978	977856.88	-121.29
-10.23346	32.707664	1042.386	977862.31	-125.77
-10.24853	32.706303	1020.867	977872.13	-120.83
-10.26204	32.717728	992.5202	977872.81	-126.18
-10.265	32.735283	966.277	977886.38	-117.55
-10.26631	32.759892	945.642	977868.38	-140.13
-10.26863	32.77739	938.9974	977874.13	-136.08
-10.26644	32.795143	911.1082	977877	-138.67
-10.27565	32.81118	902.0861	977883.88	-133.94
-10.29042	32.821548	899.8306	977888.19	-130.58
-10.30086	32.836773	906.5666	977885.63	-132.22
-10.30625	32.854561	879.5309	977888.38	-134.9
-10.30808	32.863842	870.204	977882.25	-142.94
-10.31012	32.870541	854.0801	977890.25	-138.15
-10.30703	32.888153	841.1566	977897.13	-133.69
-10.3035	32.905128	818.0222	977900.69	-134.39

Latitude (deg.)	Longitude (deg.)	Elevation (m)	Observed gravity (mGal)	Bouguer gravity (mGal)
-10.29472	32.920547	800.7401	977905.5	-132.66
-10.28433	32.935295	827.9892	977914.13	-118.46
-10.27606	32.951237	816.4068	977916.31	-118.21
-10.27137	32.967953	785.7134	977928.94	-111.3
-10.26518	32.985241	793.2115	977928.56	-109.99
-10.25828	33.002407	792.0228	977920.31	-118.17
-10.2527	33.053116	825.0326	977905.13	-126.43
-10.26167	33.066456	814.517	977906.88	-126.75
-10.27093	33.083038	840.7298	977903	-125.61
-10.27989	33.09618	855.8784	977901.44	-124.28
-10.29318	33.111008	871.6061	977899.19	-123.24
-10.30924	33.114082	894.649	977894.63	-123.93
-10.32706	33.117443	912.815	977890.69	-124.94
-10.32686	33.11747	912.5407	977876.56	-139.13
-10.35914	33.127125	948.8119	977886.81	-122.38
-10.37077	33.139381	958.0778	977892.56	-113.41
-10.37432	33.149757	1095.238	977878.81	-100.05
-10.37333	33.166439	1096.579	977857	-120
-10.36889	33.182426	1222.675	977844.13	-109.49

Latitude (deg.)	Longitude (deg.)	Elevation (m)	Observed gravity (mGal)	Bouguer gravity (mGal)
-10.36329	33.196102	1293.602	977845.94	-94.35
-10.35407	33.20845	1284.214	977830.69	-111.64
-10.34097	33.221443	1365.413	977817	-109.78
-10.32403	33.224632	1438.077	977817.06	-95.39
-10.29729	33.247566	1455.969	977809.13	-99.3
-10.28723	33.263561	1537.442	977786.63	-105.2
-10.27958	33.278725	1576.944	977785.69	-98.38
-10.27328	33.294998	1587.886	977780.69	-100.95
-10.25635	33.292229	1590.812	977782.81	-97.87
-10.23917	33.299183	1576.395	977779.88	-103.35
-10.22186	33.295052	1582.278	977773.13	-108.13

VITA

Kitso Nkooko Matende

Candidate for the Degree of

Master of Science

Thesis: MAGMATIC UNDER-PLATING BENEATH THE LUANGWA RIFT VALLEY, ZAMBIA

Major Field: Geology

Biographical:

Education:

Completed the requirements for the Master of Science in Geology at Oklahoma State University, Stillwater, Oklahoma in May, 2015.

Completed the requirements for the Bachelor of Science in Applied Geophysics at University of Botswana, Gaborone, Botswana in 2013.

Experience:

Boone Pickens School of Geology Graduate Teaching Assistant (2013 – 2015).

Attachment at DeBeers Holdings Botswana (Mid-May to Mid-July 2014).

Professional Memberships:

Society of Exploration Geophysicists (SEG)

American Geophysical Union (AGU)

European Association of Geoscientists and Engineers (EAGE)